The SCUBA Half-Degree Extragalactic Survey (SHADES) - VII. Optical/IR photometry and stellar masses of submillimetre galaxies

Journal Item

Mon. Not. R. Astron. Soc. **386,** 1107–1130 (2008) doi:10.1111/j.1365-2966.2008.13113.x

The SCUBA HAlf Degree Extragalactic Survey (SHADES) – VII. Optical/IR photometry and stellar masses of submillimetre galaxies

S. Dye,[1⋆] S. A. Eales,[1] I. Aretxaga,[2] S. Serjeant,[3] J. S. Dunlop,[4] T. S. R. Babbedge,[5] S. C. Chapman,[6] M. Cirasuolo,[4] D. L. Clements,[5] K. E. K. Coppin,[7] L. Dunne,[8] E. Egami,[9] D. Farrah,[10] R. J. Ivison,[4] E. van Kampen,[11] A. Pope,[12] R. Priddey,[13] G. H. Rieke,[9] A. M. Schael,[4] D. Scott,[12] C. Simpson,[14] T. Takagi,[15] T. Takata[16] and M. Vaccari[17]

[1]*Cardiff University, School of Physics & Astronomy, Queens Buildings, The Parade, Cardiff CF24 3AA*
[2]*Instituto Nacional de Astrofísica, Óptica y Electrónica (INAOE), Aptdo. Postal 51 y 216, 72000 Puebla, Pue., Mexico*
[3]*Astrophysics Group, Department of Physics and Astronomy, The Open University, Milton Keynes MK7 6AA*
[4]*SUPA†, Institute for Astronomy, University of Edinburgh, Royal Observatory, Edinburgh EH9 3HJ*
[5]*Astrophysics Group, Blackett Laboratory, Imperial College, Prince Consort Road, London SW7 2BW*
[6]*Institute of Astronomy, University of Cambridge, Madingley Road, Cambridge CB3 0HA*
[7]*Institute for Computational Cosmology, Department of Physics, Durham University, Durham DH1 3LE*
[8]*The School of Physics & Astronomy, University of Nottingham University Park, Nottingham NG7 2RD*
[9]*Steward Observatory, University of Arizona, 933 N. Cherry Avenue, Tuscon, AZ 85721, USA*
[10]*Department of Astronomy, 610 Space Sciences Building, Cornell University, Ithaca, NY 14853, USA*
[11]*Institute for Astro- and Particle Physics, University of Innsbruck, Technikerstrasse 25, A-6020 Innsbruck, Austria*
[12]*Department of Physics & Astronomy, University of British Columbia, Vancouver, BC, Canada V6T 1Z1*
[13]*Centre for Astrophysics Research, University of Hertfordshire, Hatfield AL10 9AB*
[14]*Astrophysics Research Institute, Liverpool John Moores University, Egerton Wharf, Birkenhead CH41 1LD*
[15]*Institute of Space and Astronautical Science, Yoshinodai 3-1-1, Sagamihara, Kanagawa 229 8510, Japan*
[16]*National Astronomical Observatory of Japan, 650 North A'ohoku Place, Hilo, HI 96720, USA*
[17]*Department of Astronomy, Vicolo dell'Osservatorio 3, University of Padova, I-35122 Padova, Italy*

Accepted 2008 February 14. Received 2008 February 4; in original form 2007 September 7

ABSTRACT

We present estimates of the photometric redshifts, stellar masses and star formation histories of sources in the Submillimetre Common-User Bolometer Array (SCUBA) HAlf Degree Extragalactic Survey (SHADES). This paper describes the 60 SCUBA sources detected in the Lockman Hole covering an area of ∼320 arcmin^2. Using photometry spanning the *B* band to 8 μm, we find that the average SCUBA source forms a significant fraction of its stars in an early period of star formation and that most of the remainder forms in a shorter more intense burst around the redshift it is observed. This trend does not vary significantly with source redshift. However, the sources show a clear increase in stellar mass with redshift, consistent with downsizing. In terms of spectral energy distribution types, only two out of the 51 sources we have obtained photometric redshifts for are best fitted by a quasar-like spectrum, with approximately 80 per cent of the sources being best fitted with late-type spectra (Sc, Im and starburst). By including photometry at 850 μm, we conclude that the average SCUBA source is forming stars at a rate somewhere between 6 and 30 times the rate implied from the rest-frame optical in a dust obscured burst and that this burst creates 15–65 per cent of the total stellar mass. Using a simplistic calculation, we estimate from the average star formation history that between one in five and one in 15 bright ($L_* + 2 < L_{\rm optical} < L_* - 1$ mag) galaxies in the field over the interval $0 < z < 3$ will at some point in their lifetime

⋆E-mail: s.dye@astro.cf.ac.uk
†Scottish Universities Physics Alliance.

experience a similar energetic dusty burst of star formation. Finally, we compute the evolution of the star formation rate density and find it peaks around $z \sim 2$.

Key words: surveys – galaxies: evolution – galaxies: high-redshift – cosmology: observations – infrared: galaxies – submillimetre.

1 INTRODUCTION

The Submillimetre Common-User Bolometer Array (SCUBA) HAlf Degree Extragalactic Survey (SHADES) is a wide area extragalactic submillimetre (submm) survey conducted with SCUBA (Holland et al. 1999). The motivation for SHADES is discussed at length in the survey definition paper by Mortier et al. (2005). The survey comprises two separate fields of approximately equal area, one in the Lockman Hole and one in the Subaru/*XMM–Newton* Deep Field (SXDF). Up to the time of decommissioning of SCUBA in 2005, SHADES had acquired approximately 40 per cent of the target area to the proposed depth of 2 mJy, culminating in the detection of a total of 120 robust SCUBA sources over $\sim$650 arcmin^2 (Coppin et al. 2006).

SHADES satisfies a long-awaited demand for a large, homogeneous sample of submm sources with multiwavelength follow-up data. Since their detection in the first deep submm surveys (Smail, Ivison & Blain 1997; Barger et al. 1998; Hughes et al. 1998), much has been learnt about the dusty high-redshift sources revealed by SCUBA. However, several major questions regarding this elusive population remain unanswered.

Arguably the most important question is the relationship between SCUBA sources and present-day galaxies. Several clues point towards a strong link with massive low-redshift ellipticals, such as their similar comoving number densities (Scott et al. 2002; Dunne, Eales & Edmunds 2003), clustering properties (e.g. Almaini et al. 2003; Blain et al. 2004) and their typically very high star formation rates (SFRs) which enable the rapid formation of a large stellar system. If this link is valid, then an immediate question that arises is at what stage of this transformation do we observe the object as a SCUBA galaxy? It is possible that there is more than one answer if multiple routes exist to the same type of final massive elliptical. For example, the average elliptical's entire stellar population may either form in a single large burst or in a series of smaller bursts triggered by mergers.

Crucial evidence can be provided by the star formation history (SFH) of the average SCUBA source. However, in order to establish an SFH, several ingredients are needed: (1) the source must be identified from its somewhat imprecise SCUBA position, (2) multiwavelength data (ideally covering optical to submm) must be acquired and (3) the source's redshift must be known. Deep radio surveys (e.g. Ivison et al. 2002) detect somewhere between a half and three-quarters of SCUBA sources to give precise positional information. In addition, SCUBA sources can be efficiently identified with relatively short exposures using the *Spitzer Space Telescope* (*Spitzer*) as demonstrated by several authors (e.g. Egami et al. 2004; Huang et al. 2004). Once accurate positions have been obtained, optical spectroscopy can then be carried out.

Unfortunately, this procedure has several selection effects. The requirement that a source be detected at radio wavelengths can lead to a lack of sources at high redshifts ($z \gtrsim 3$) where the radio flux falls below the detection limit (see e.g. Chapman et al. 2005). There is also a paucity of sources at redshifts where no bright spectral features fall within the optical waveband, particularly over the redshift interval $1.2 < z < 1.9$ (the 'redshift desert'). Photometric redshifts, albeit less precise, do not suffer from the latter selection effect. Another advantage is that contaminating flux from near-neighbours and blended sources (as an appreciable fraction of SCUBA sources appear to be) is more readily quantified in image data unlike spectroscopic data where small uncertainties in the slit placement can lead to ambiguities in deblending.

In this paper, we make use of photometric redshifts to investigate the photometric properties, stellar masses and SFHs of SCUBA sources in SHADES. Counterparts are identified through either deep radio data or *Spitzer* 24-μm images. Having the option of a 24-μm identification means that the SCUBA sources considered in this work are not entirely subject to the strong radio selection function (although it may be contended that the process of identifying counterparts in the radio is more physically motivated).

This paper is seventh in a series of papers arising from SHADES. Paper I by Mortier et al. (2005) describes the science goals, motivation and strategy. Paper II (Coppin et al. 2006) presents the maps, catalogues and source counts and describes the data reduction. Paper III (Ivison et al. 2007) details the radio follow-up of the SHADES areas and identifies the radio and 24-μm *Spitzer* counterparts to the SHADES sources. Paper IV (Aretxaga et al. 2007) derives photometric redshifts of the SHADES sources using radio, submm and far-infrared (far-IR) data. Paper V (Takagi et al. 2007) concerns the submm properties of near-IR selected galaxies in the SXDF. Paper VI (Coppin et al. 2007) presents 350-μm observations of a subset of SHADES sources. Papers VII (this paper) and VIII (Clements et al., in preparation) form a pair split by survey area: Paper VII considers photometric redshifts, stellar masses and SFHs of sources in the Lockman Hole whereas Paper VIII is concerned with photometric redshifts in the SXDF. Papers VII and VIII are divided primarily due to data propriety, but also because of different optical and near-IR coverage between the two areas. In terms of forthcoming papers, Paper IX (Serjeant et al., in preparation) will investigate stacking of the SHADES data to statistically determine properties of the very faint sources hidden in the noise. Paper X (van Kampen et al., in preparation) will study the clustering of SHADES sources. Finally, several further SHADES publications are anticipated concerning 1.1-mm data acquired with the AzTEC instrument on the James Clerk Maxwell Telescope.

The layout of this paper is as follows. Section 2 outlines the acquisition and reduction of data used in this work. Section 3 discusses the results of our photometric redshift analysis and properties of the spectral energy distributions (SEDs). In Section 4, we describe our method of obtaining stellar masses together with the resulting masses, SFRs and evolution of the SFR density. We conclude the main paper sections with a summary and discussion in Section 5. We provide three appendices: Appendix A contains multiwavelength postage stamp images for each of our sources as well as their best-fitting SEDs, Appendix B provides descriptions for a selection of noteworthy sources and Appendix C lists the photometry for all sources.

Throughout this paper, we assume the following cosmology: $H_0 = 70\,\mathrm{km\,s^{-1}\,Mpc^{-1}}, \Omega_\mathrm{m} = 0.3, \Omega_\Lambda = 0.7$.

2 DATA

2.1 SHADES catalogue and counterparts

The sources investigated in this paper were extracted from 850-μm SCUBA observations of the Lockman Hole centred on RA = $10^\mathrm{h}52^\mathrm{m}26\overset{\mathrm{s}}{.}7$, Dec. = $57^\circ24'12\overset{''}{.}6$ (J2000). The Lockman Hole data cover an area of $\sim$320 arcmin^2 to an rms noise level of $\sim$2 mJy. To ensure a robust list of SCUBA sources, the map reduction and catalogue generation was carried out by four independent groups within the SHADES consortium. Only sources with a signal-to-noise ratio (S/N) of $\geqslant$3 (before deboosting) in at least two reductions were retained. This left a total of 60 sources in the Lockman Hole field with a probability of <5 per cent of being spurious. For more specific details on the reduction of the SCUBA map and source extraction, the reader is referred to Coppin et al. (2006).

Follow-up 1.4-GHz imaging with the Very Large Array and 24-μm imaging with *Spitzer* are described in Ivison et al. (2007). Potential radio and 24-μm counterparts to the SCUBA sources were searched for within a radius of 8 arcsec and the significance of each match quantified using the method of Downes et al. (1986). This method gives the probability, P, of a counterpart being associated with the SCUBA position by chance based on the separation and the number counts. In this way, a counterpart either in the radio or at 24 μm is defined as being robust if its distance from the SCUBA position is less than 8 arcsec and $P \leqslant 0.05$. Non-robust identifications are defined as those with $P > 0.05$ within 8 arcsec or those that lie within an extended search radius $8 < r < 12.5$ arcsec in the radio or $8 < r < 15$ arcsec at 24 μm.

Ivison et al. (2007) lists several counterparts for many of the SHADES sources. In the present work, we base our analysis on the single, most likely counterpart for each source. We define these 'primary counterparts' as those with the lowest value of P in the radio or at 24 μm (often both). Although not included in any of our later analyses, for completeness, we also compute photometric redshifts for secondary counterparts. A secondary counterpart is defined as having a robust 24 μm and/or robust radio identification but with a numerically higher P than the primary. These are listed in Table 2 alongside the primary counterparts. In all cases, the coordinates listed in Table 2 are either the radio or 24-μm coordinates given in Ivison et al. (2007) depending on which identification has the lowest P. (There is one exception: Lock850.036 for which we give the SCUBA 850-μm centroid since this source has no radio or 24-μm counterparts.)

2.2 Optical and near-IR photometry

Our optical images in B, R, I and z were obtained with SuprimeCam (Miyazaki et al. 2002) on the Subaru telescope in 2006 January. The images fully cover the Lockman area observed by SCUBA and reach a 5σ point source sensitivity of 26.8, 25.8, 25.7 and 25.0 mag (AB) in B, R, I and z, respectively, as measured in a 3 arcsec diameter aperture. Total exposure times for B, R, I and z are, respectively, 7200, 3360, 4730 and 4800 s. The seeing in the images varies from 0.66 to 0.84 arcsec between bands with a mean of 0.76 arcsec.

Our K-band image was obtained with the Wide Field Camera (WFCAM) on the United Kingdom Infrared Telescope (UKIRT). The data were taken as part of the Deep Extragalactic Survey, one of the five projects comprising the UKIRT Deep Infrared Sky Survey (UKIDSS Lawrence et al. 2006). The image is a mosaic of four separate quadrants observed in array number 1 (see Dye et al. 2006, for further details). The exposure time of the four quadrants varies between 9180 and 11 460 s, reaching an average 5σ point source sensitivity of 22.9 mag (AB) (Warren et al. 2007).

We used SEXTRACTOR (Bertin & Arnouts 1996) to extract sources from the optical and K-band data. Only objects with five or more interconnecting pixels lying above a threshold S/N of 2σ were extracted. Fluxes were computed within a 3 arcsec diameter aperture.

2.3 *Spitzer* photometry

Spitzer's Infrared Array Camera (IRAC; Fazio et al. 2004) was used to obtain images at wavelengths 3.6, 4.5, 5.8 and 8 μm. The integration time for each image was 500 s, reaching 5σ point source detection limits of 1.3, 2.7, 18 and 22 μJy for 3.6, 4.5, 5.8 and 8 μm, respectively. The data were reduced using the Spitzer Science Centre (SSC) pipeline (Gordon et al. 2005).

The pipeline produces the total flux of each source. To match the total flux of a given source in each of the IRAC bands to the optical and near-IR 3-arcsec photometry accounting for the different point spread functions (PSFs), we adopted the following procedure: (1) fit a 2D Gaussian to the source in the IRAC image, (2) scale the fitted Gaussian to the size it would have been if it had been observed with the SuprimeCam PSF, (3) compute the flux within a 3 arcsec diameter aperture centred on the scaled Gaussian using the total flux output by the IRAC pipeline. The average of all corrections across all bands and sources[1] was +0.34 mag with a 1σ scatter of 0.15 mag. To account for possible systematics introduced by this scheme, we added an error of 0.15 mag in quadrature to the error computed by the SSC pipeline for all IRAC photometry.

In addition to IRAC imaging of the Lockman Hole, data were taken using the multiband photometer for *Spitzer* (MIPS; Rieke et al. 2004). Although we do not use MIPS fluxes directly in the present work, our identification of counterparts to the SCUBA sources relies on 24-μm MIPS detections (see previous section and also Ivison et al. 2007).

2.4 Cross-matching procedure

To obtain the multiwavelength list for all the SHADES counterparts, the sources on the different images were position coincidence matched using a tolerance of 1 arcsec. All matches were carefully verified by eye to correct for obvious mismatches, spurious detections and blended photometry. In cases where blended photometry was identified, we adjusted the deblending threshold and cleaning parameter in SEXTRACTOR on a source by source basis until deblended photometry was obtained.

3 PHOTOMETRIC REDSHIFTS AND SPECTRA

3.1 Method of determination

We obtained photometric redshifts for the SHADES sources by applying the HYPERZ redshift code (Bolzonella, Miralles & Pelló 2000) to our nine-band photometry (B, R, I, z, K, 3.6, 4.5, 5.8 and 8 μm) de-

[1] Since the correction applies to the total flux which is practically insensitive to the PSF and since sources are effectively brought to the same seeing in each IRAC waveband, the scatter in the correction between wavebands for a given source is primarily due to the image noise and wavelength dependent source morphology, not the varying PSF between wavebands.

scribed in the previous section. The template galaxy SEDs packaged with HYPERZ are based on the local SEDs measured by Coleman, Wu & Weedman (1980), with an extrapolation into the IR using the results of spectral synthesis models. The lack of any empirical basis for these templates at wavelengths >1 μm is clearly unsatisfactory since our photometry includes both near-IR and mid-IR measurements. Therefore, we constructed our own set of templates. Mannucci et al. (2001) list empirical SEDs over the wavelength range 0.1–2.4 μm for the Hubble types E, S0, Sa, Sb and Sc. We extended these out to 10 μm using the average SEDs for disc galaxies and elliptical galaxies listed in table 3 of Lu et al. (2003).

One disadvantage of these templates is the lack of a template for an irregular galaxy, and we therefore retained the HYPERZ Im template, extending this into the mid-IR using the average disc–galaxy SED from Lu et al. (2003). In terms of the variation in SED shape, particularly the average slope between $0.2 < \lambda < 2$ μm, the jump from the Sc template to the Im template is larger than the progression through the earlier type SEDs. Therefore, we introduced a seventh intermediate template with a composition of 60 per cent Sc and 40 per cent Im to bridge this jump.

Finally, we introduced a starburst (SB) and quasar (QSO) template. For the SB template, we extended the spectrum of Kinney et al. (1996) to longer and shorter wavelengths using a Bruzual & Charlot (2003) spectrum corresponding to a 0.1-Gyr duration starburst as observed at the end of that time. Since this extension lacks the dusty spectral features seen in the mid-IR, we added these from the spectra of Lu et al. (2003). The QSO template was taken from Brotherton et al. (2001) and extended longward of 7500 Å using the QSO spectrum of Elvis et al. (1994). This is an average SED and therefore does not cater for a variable power-law slope. Similarly, we chose not to include templates containing a mix of QSO and starburst activity. Our preference is for a more clear-cut approach: The QSO template that we use is sufficiently different from the other templates to be well suited for picking out obvious QSO candidates.

The nine SED templates are plotted in Fig. 1. Throughout this paper, we refer to SED templates by their number: 1 = E, 2 = S0, 3 = Sa, 4 = Sb, 5 = Sc, 6 = Sc + Im, 7 = Im, 8 = starburst, 9 = QSO.

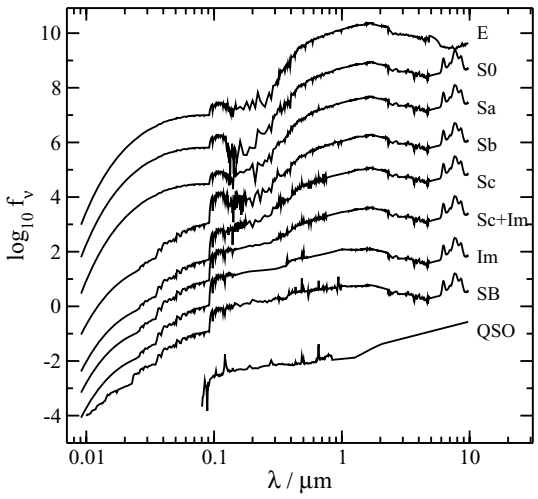

Figure 1. Template SEDs used with HYPERZ for determination of the photometric redshifts. The template Sc + Im is a hybrid SED composed of 60 per cent Sc and 40 per cent Im to bridge the jump between the Sc and Im types (see text). SED templates are referred to throughout this paper by their number: 1 = E, 2 = S0, 3 = Sa, 4 = Sb, 5 = Sc, 6 = Sc + Im, 7 = Im, 8 = starburst, 9 = QSO.

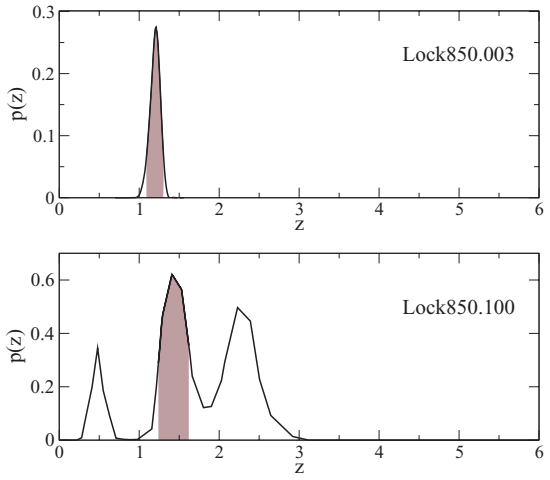

Figure 2. Two extreme examples of the photometric redshift probability distribution of the SHADES sources studied in this paper. The top panel corresponds to the source Lock850.003 which has a very robust photometric redshift. Conversely, the bottom panel corresponds to Lock850.100 which has three almost equally likely photometric redshifts. The grey-shaded area indicates the 90 per cent confidence range in primary z as given in Table 2.

To determine the redshifts, we allowed HYPERZ to search over the range $0 < z < 6$. We used a Calzetti reddening law to account for dust extinction, allowing the rest-frame V-band attenuation, A_V, to vary from 0 to 5 mag in steps of 0.1 mag (requiring recompilation of HYPERZ with a larger array). No cut-off was imposed on the absolute K-band magnitude (AB) computed by HYPERZ (see Section 4) although we imposed a minimum magnitude error of 0.05 mag for all filters to account for zero-point errors. We configured HYPERZ to treat non-detected sources as having zero flux with a 1σ error equal to the flux sensitivity of the corresponding filter. (We also tried a more stringent configuration whereby the error is set to half the sensitivity with negligible effect on the results.) All filter transmission profiles were modified where appropriate to account for the wavelength-dependent quantum efficiency of the detector, the mirror reflectivity and atmospheric attenuation.

We note that we include the quantity $p(z)$ in Table 2 and its corresponding $p(z2)$ for secondary redshifts. This quantity is the integral of the area under the peak of the redshift probability distribution normalized by the total area within $0 < z < 6$ for a given source. The redshift probability distribution is computed from the χ^2 curve output by HYPERZ. The most likely redshift (i.e. lowest χ^2) is taken as the primary solution, not the peak with the largest enveloped area. Fig. 2 shows $p(z)$ versus z for two extreme cases in Table 2. At one extreme is Lock850.003 where a very robust photometric redshift with a small error and no secondary solution is obtained and at the other extreme is Lock850.100 where three almost equally likely solutions exist. We find that the majority of sources have a single well-defined peak.

3.2 Photometric redshifts and SED results

3.2.1 Photometric redshifts

Table 2 lists the photometric redshifts obtained for 51 primary counterparts (and 12 secondary counterparts) of the 60 SHADES sources and the lower plot in Fig. 3 shows their distribution. The best-fitting SEDs are shown in Fig. A1. The median redshift of the sample is $z = 1.52$ in close agreement with the median photometric redshift

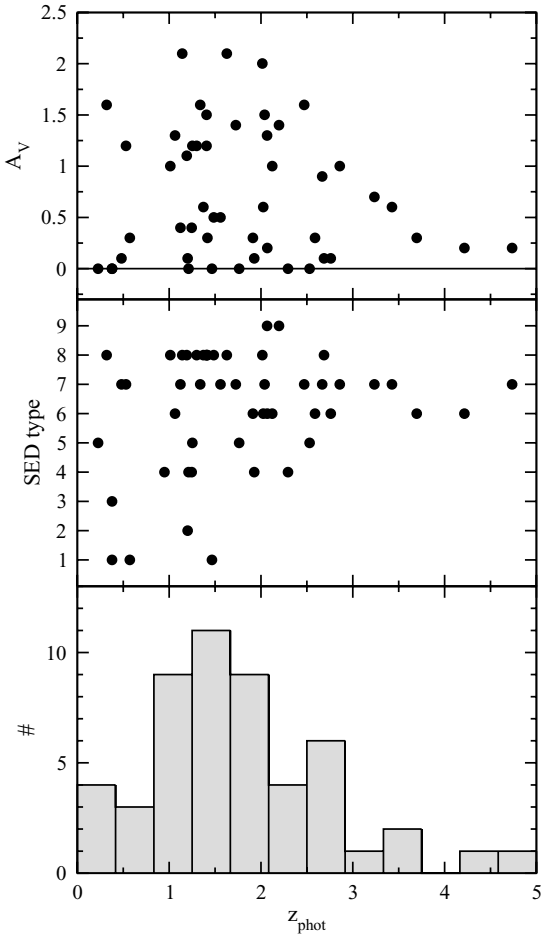

Figure 3. Bottom panel: Histogram of photometric redshifts computed for the 51 primary SHADES sources listed in Table 2. Middle panel: Variation of SED type with redshift. Top panel: Variation of attenuation by dust with redshift.

measured in the SHADES SXDF field by Clements et al. (in preparation). Redshifts for nine of the sources could not be determined due to insufficient photometric points (either because they are too faint and therefore not detected at certain wavelengths – we stipulate a minimum of three fluxes per source to determine a redshift – or because they are heavily blended with a neighbouring source).

A simple measure of the appropriateness of our SED templates to the photometry is the distribution of χ^2. This depends on the accuracy of our photometric errors although for simple aperture fluxes, these are reliably determined. The distribution for all our SED fits is perfectly consistent with a χ^2 distribution of five degrees of freedom. This is as it should be for nine photometric constraints (including upper limits) and four fitted parameters (z, A_V, SED normalization and SED type) implying that our SED template set provides a suitable match to the SCUBA sources.

We have compared the photometric redshifts output by HYPERZ with three alternative determinations (see Table 1 for a summary). First, still applying HYPERZ but using the synthetic spectra of Bruzual & Charlot (2003) packaged with it, we found generally good agreement although a slightly larger spread in the distribution of χ^2. Secondly, we used the *BPZ* code of Benitez (2000) with our own SED templates. Although this code does not allow for attenuation by dust, it uses a Bayesian approach incorporating a luminosity prior. We set the prior to the luminosity function obtained from the *Hubble Deep Field*-North and found excellent agreement with the results of HYPERZ when no dust attenuation was included. However, the inclusion of dust attenuation in HYPERZ gives significantly different redshifts for a large fraction of the sources and values of χ^2 that are a factor of two times lower on average. As expected, this shows that dust has a significant effect on the SEDs of the SCUBA sources (also reflected in the values of A_V seen in Table 2).

Table 1. Comparison of the different photometric redshifts (photo-zs) considered in Section 3.2.1. $\langle\sigma_z\rangle$ is the median 1σ uncertainty in the photo-zs of all 60 SHADES sources and $\langle|\Delta z|\rangle$ is the median absolute difference between the photo-zs listed in Table 2 and the others discussed. The photo-z types listed are: HYPERZ – the photo-zs in Table 2, i.e. obtained using HYPERZ with the empirical SED templates discussed in Section 3.1; HYPERZ + BC – again using HYPERZ but with the Bruzual & Charlot (2003) SED templates; *BPZ* – using the code by Benitez (2000) with the emperical SED templates of Section 3.1; SFH – our own photo-zs from the SFH analysis of Section 4.1; submm – the photo-zs of Aretxaga et al. (2007).

Photo-z type	$\langle\|\Delta z\|\rangle$	$\langle\sigma_z\rangle$
HYPERZ	–	0.10
HYPERZ + BC	0.34	0.14
BPZ	0.21	0.31
SFH	0.18	0.16
submm	0.78	0.60

In the third and final case, we compared the HYPERZ redshift estimates with our own photometric redshifts obtained using the SFH analysis presented in Section 4.1. Fig. 4 shows the comparison. The agreement is very good with an average $|\Delta z|/(1+z)$ of 0.09 [for comparison, the average $\sigma_z/(1+z)$ for the HYPERZ redshifts is 0.06]. Since the two methods are completely independent, with one using empirical SED template fitting and the other synthetic spectra constructed from a best-fitting SFH, this supports the reliability of our redshifts.

Unfortunately, there are very few SCUBA sources in the Lockman Hole with robust spectroscopic redshifts against which we can compare our photometric redshifts. Nevertheless, in Fig. 5 we show a comparison with the seven that currently exist. The only irreconcilable discrepancy is Lock850.017 with $z_{\rm phot} = 1.06^{+0.24}_{-0.06}$ and $z_{\rm spec} = 2.24$. The optical counterpart to this source coincides exactly with the radio and spectroscopic position, is not blended with any neighbours and is detected with a very high S/N at all wavelengths. The photometry is extremely well fitted by the Im + Sc template with a reduced χ^2 of 0.28 ± 0.10 and a single sharp peak in the probability distribution of the fit. However, the optical morphology shows a relatively diffuse tail extending $\sim$3 arcsec to the south-west of the nucleus of this source. A possible cause of the discrepancy could therefore be that there are two closely aligned objects at different redshifts. Our photometry is dominated by the compact nucleus which could be a foreground source, whereas the spectroscopic redshift could be based on emission lines from the more diffuse background source.

We draw particular attention to the interesting source Lock850.041b. The radio coordinates of this source correspond to the brightest but slightly less favourable of two radio sources within 8 arcsec of the SCUBA centroid. Ivison et al. (2005) were unable to measure a spectroscopic redshift at the radio coordinates of Lock850.041b but did measure a spectroscopic redshift of $z = 0.69$ for an elliptical galaxy lying $\sim$2 arcsec to the south-west of the radio

Table 2. Photometric redshifts of the Lockman Hole SHADES sources. Those sources with an ID suffix 'b' are the secondary counterparts listed here for completeness but discounted from all analysis (see Section 2.1). Codes in column labelled 'C' indicate whether the source has a radio and/or 24-μm counterpart. First character corresponds to radio and second to 24 μm with 'R' indicating a robust identification, 'N' a non-robust identification and '–' no detection (see Section 2.1). All coordinates are either the radio or 24-μm coordinates from Ivison et al. (2007) depending on which is the more likely identification (exception is Lock850.036 – see text). Columns z^+ and z^- give the 90 per cent uncertainty range on the photometric redshift, z. Column 'SED' lists best-fitting template number (see text). Absolute AB magnitude listed under M_K. χ^2 of the SED fit and the fractional area contained under the peak of the probability distribution for χ^2, $p(z)$, are given in columns 11 and 12 (see text). Columns 13–15 list secondary redshift solutions and their corresponding χ^2 and p. Last column gives spectroscopic redshifts from either (1) Ivison et al. (2005) or (2) Chapman et al. (2005) (robust redshifts in bold).

ID	C	RA	Dec.	z	z^-	z^+	SED	A_V	M_K	$\chi^2(z)$	$p(z)$	$z2$	$\chi^2(z2)$	$p(z2)$	$z_{\rm spec}$
Lock850.001	RR	10 52 01.249	+57 24 45.76	4.21	2.41	4.45	6	0.2	−24.15	0.76	0.87	–	–	–	2.15[1]
Lock850.002	RR	10 52 57.084	+57 21 02.82	3.23	2.76	3.34	7	0.7	−24.10	0.22	0.98	–	–	–	–
Lock850.003	RR	10 52 38.299	+57 24 35.76	1.21	1.12	1.25	4	0.0	−22.91	0.69	1.00	–	–	–	3.04[1]
Lock850.003b	RR	10 52 38.401	+57 24 39.50	1.51	1.24	1.61	2	0.1	−23.36	0.99	0.36	0.71	1.02	0.37	–
Lock850.004	RR	10 52 04.079	+57 26 58.52	2.66	2.25	2.85	7	0.9	−24.71	0.26	0.73	3.16	0.73	0.26	0.53[1]
Lock850.004b	RN	10 52 04.226	+57 26 55.46	2.11	1.59	2.50	6	0.9	−24.26	0.67	1.00	–	–	–	**1.48**[1]
Lock850.005	−N	10 53 02.696	+57 18 21.95	1.20	0.87	1.24	2	0.1	−22.96	0.52	0.96	–	–	–	–
Lock850.006	RR	10 52 04.013	+57 25 24.20	2.01	1.81	3.18	8	2.0	−23.67	0.60	0.98	–	–	–	–
Lock850.007	RR	10 53 00.956	+57 25 52.06	–	–	–	–	–	–	–	–	–	–	–	–
Lock850.008	−R	10 51 53.690	+57 18 34.90	–	–	–	–	–	–	–	–	–	–	–	–
Lock850.009	RR	10 52 15.636	+57 25 04.26	1.62	1.54	1.87	8	2.1	−23.88	0.75	0.97	–	–	–	**1.85**[1]
Lock850.009b	−R	10 52 15.730	+57 25 01.70	0.91	0.82	1.01	6	0.4	−23.01	0.43	1.00	–	–	–	–
Lock850.010	R–	10 52 48.992	+57 32 56.26	–	–	–	–	–	–	–	–	–	–	–	–
Lock850.010b	−N	10 52 48.270	+57 32 51.00	1.33	1.26	1.39	7	1.1	−22.09	0.91	0.98	–	–	–	–
Lock850.011	−N	10 51 29.160	+57 24 06.80	1.33	1.23	1.42	7	1.6	−21.99	0.32	0.64	1.75	0.58	0.36	–
Lock850.012	RR	10 52 27.579	+57 25 12.46	2.03	1.83	2.33	7	1.5	−24.07	0.75	0.93	2.77	1.56	0.07	2.14[1]
Lock850.013	−N	10 51 31.770	+57 31 41.20	0.48	0.31	0.55	7	0.1	−21.70	0.61	1.00	–	–	–	–
Lock850.014	NN	10 52 30.717	+57 22 09.56	2.76	2.47	3.08	6	0.1	−25.17	0.45	0.81	1.97	0.89	0.19	**2.61**[1]
Lock850.015	RR	10 53 19.271	+57 21 08.45	2.53	2.08	2.94	5	0.0	−24.24	1.45	0.99	–	–	–	–
Lock850.015b	R–	10 53 19.025	+57 21 09.47	–	–	–	–	–	–	–	–	–	–	–	–
Lock850.016	RR	10 51 51.690	+57 26 36.09	1.25	1.05	1.38	5	1.2	−24.26	0.65	0.88	0.71	1.31	0.12	**1.15**[1]
Lock850.017	RR	10 51 58.018	+57 18 00.27	1.12	1.00	1.38	6	1.3	−23.39	0.28	1.00	–	–	–	**2.24**[1]
Lock850.017b	−R	10 51 58.480	+57 18 01.20	0.36	0.30	0.44	8	2.1	−17.91	3.55	0.69	0.15	3.98	0.29	–
Lock850.018	R–	10 52 27.778	+57 22 18.18	–	–	–	–	–	–	–	–	–	–	–	1.96[1]
Lock850.019	−R	10 52 36.090	+57 31 19.60	3.69	3.56	3.75	6	0.3	−24.35	3.56	0.88	3.00	4.30	0.11	–
Lock850.021	−R	10 52 56.790	+57 30 37.90	0.94	0.43	3.24	4	4.9	−21.13	0.08	0.90	0.22	0.77	0.07	–
Lock850.022	−R	10 51 37.090	+57 33 16.90	2.68	2.55	2.90	8	0.1	−24.11	0.89	0.93	1.86	2.24	0.07	–
Lock850.023	−N	10 52 14.976	+57 31 53.62	0.57	0.53	0.68	1	0.3	−23.28	1.67	1.00	–	–	–	–
Lock850.024	RR	10 52 00.445	+57 20 40.16	1.40	1.25	1.49	8	1.5	−24.12	0.72	1.00	–	–	–	–
Lock850.026	RR	10 52 40.698	+57 23 09.96	2.86	1.84	3.19	7	1.0	−23.43	1.11	0.98	–	–	–	–
Lock850.027	−N	10 52 03.450	+57 18 19.30	1.12	1.03	1.20	7	0.4	−22.47	1.17	1.00	–	–	–	–
Lock850.028	NN	10 52 57.667	+57 30 58.71	1.14	1.08	1.20	8	2.1	−23.29	0.35	1.00	–	–	–	–
Lock850.029	N–	10 51 31.305	+57 20 40.28	–	–	–	–	–	–	–	–	–	–	–	–
Lock850.030	RR	10 52 07.490	+57 19 04.01	2.06	1.85	2.56	6	0.2	−23.01	0.74	0.82	0.52	1.47	0.17	**2.69**[2]
Lock850.031	RR	10 52 15.989	+57 16 19.34	2.12	1.95	2.31	6	1.0	−24.44	0.81	1.00	–	–	–	–
Lock850.033	RN	10 51 55.470	+57 23 12.77	2.58	1.98	2.98	6	0.3	−23.35	0.38	0.55	1.08	0.83	0.33	**2.66**[1]
Lock850.034	RN	10 52 14.202	+57 33 28.30	3.42	3.15	3.69	7	0.6	−24.05	0.92	1.00	–	–	–	–
Lock850.035	N–	10 52 46.655	+57 20 52.54	–	–	–	–	–	–	–	–	–	–	–	–
Lock850.035b	−N	10 52 45.940	+57 20 51.40	1.59	1.41	1.71	7	0.6	−22.68	1.03	1.00	–	–	–	–
Lock850.036	–	10 52 09.335	+57 18 06.78	–	–	–	–	–	–	–	–	–	–	–	–
Lock850.037	R–	10 51 24.342	+57 23 36.18	–	–	–	–	–	–	–	–	–	–	–	–
Lock850.037b	NR	10 51 24.595	+57 23 31.08	1.51	1.46	1.66	8	1.7	−23.61	1.01	1.00	–	–	–	–
Lock850.038	RR	10 53 07.060	+57 24 31.60	1.29	1.17	1.39	8	1.2	−23.67	0.85	1.00	–	–	–	–
Lock850.039	–	10 52 25.505	+57 16 08.54	–	–	–	–	–	–	–	–	–	–	–	–
Lock850.040	RN	10 52 01.721	+57 19 17.00	2.02	1.87	2.14	6	0.6	−23.88	2.92	0.98	–	–	–	–
Lock850.041	RR	10 51 59.760	+57 24 24.94	1.01	0.91	1.11	8	1.0	−24.13	2.02	1.00	–	–	–	–
Lock850.041b	RR	10 52 00.248	+57 24 21.69	2.22	2.05	2.44	9	0.9	−24.37	0.86	0.52	0.32	1.17	0.26	–
Lock850.043	NR	10 52 56.561	+57 23 52.80	1.72	1.67	1.91	7	1.4	−23.49	0.99	1.00	–	–	–	–
Lock850.043b	NR	10 52 56.576	+57 23 58.62	1.14	1.04	1.42	8	1.4	−23.96	0.39	1.00	–	–	–	–
Lock850.047	−N	10 52 34.850	+57 25 04.60	0.37	0.33	0.42	1	0.0	−20.21	4.49	0.91	3.97	4.80	0.09	–
Lock850.048	−R	10 52 56.030	+57 32 42.30	0.31	0.24	0.37	8	1.6	−21.28	0.81	1.00	–	–	–	–
Lock850.052	RR	10 52 45.808	+57 31 19.86	1.24	1.15	1.30	4	0.4	−24.00	0.66	0.57	0.96	0.96	0.43	–
Lock850.052b	−R	10 52 46.160	+57 31 20.20	1.40	1.28	1.60	5	1.5	−23.62	0.81	0.84	0.71	1.63	0.12	–
Lock850.053	−R	10 52 40.290	+57 19 24.40	1.55	1.45	1.74	7	0.5	−23.19	1.22	1.00	–	–	–	–
Lock850.060	−N	10 51 43.900	+57 24 43.60	1.92	1.12	2.34	4	0.1	−22.38	1.11	0.60	2.69	1.37	0.16	–

Table 2 – *continued*

ID	C	RA	Dec.	z	z^-	z^+	SED	A_V	M_K	$\chi^2(z)$	$p(z)$	$z2$	$\chi^2(z2)$	$p(z2)$	$z_{\rm spec}$
Lock850.063	RR	10 51 54.261	+57 25 02.55	4.73	4.62	4.89	7	0.2	−25.50	0.14	1.00	–	–	–	–
Lock850.064	NN	10 52 52.320	+57 32 33.00	1.19	1.11	1.36	8	1.1	−22.45	0.29	1.00	–	–	–	–
Lock850.066	−N	10 51 39.570	+57 20 27.10	1.41	1.01	1.94	8	0.3	−20.70	0.05	0.54	2.15	0.27	0.33	–
Lock850.067	−R	10 52 08.870	+57 23 56.30	1.46	1.33	1.80	1	0.0	−21.89	0.71	1.00	–	–	–	–
Lock850.070	NN	10 51 47.894	+57 30 44.37	0.53	0.46	0.62	7	1.2	−20.86	0.84	1.00	–	–	–	–
Lock850.071	RN	10 52 19.086	+57 18 57.87	1.91	1.76	2.07	6	0.3	−23.18	1.44	1.00	–	–	–	–
Lock850.073	RR	10 51 41.992	+57 22 17.52	1.40	1.31	1.50	8	1.2	−23.76	0.16	1.00	–	–	–	–
Lock850.073b	R–	10 51 41.705	+57 22 20.10	1.64	1.45	1.79	6	0.1	−23.33	1.22	1.00	–	–	–	–
Lock850.075	−N	10 53 15.190	+57 26 45.90	2.06	1.95	2.28	9	1.3	−23.87	0.77	0.55	0.29	1.07	0.35	–
Lock850.076	RR	10 51 49.101	+57 28 40.28	0.37	0.27	0.42	3	0.0	−22.39	1.55	1.00	–	–	–	–
Lock850.077	RR	10 51 57.153	+57 22 09.58	1.76	1.68	1.88	5	0.0	−21.96	1.27	0.65	1.34	1.58	0.34	–
Lock850.077b	RN	10 51 57.665	+57 22 12.35	1.02	0.99	1.13	5	1.2	−23.37	6.08	1.00	–	–	–	–
Lock850.078	−N	10 51 44.088	+57 17 44.52	1.48	1.39	1.85	8	0.5	−21.73	0.08	0.39	0.58	0.23	0.31	–
Lock850.079	NR	10 51 52.594	+57 21 24.43	2.29	2.13	2.43	4	0.0	−24.58	4.33	1.00	–	–	–	–
Lock850.081	NN	10 52 31.523	+57 17 51.67	2.19	2.07	2.37	9	1.4	−27.51	2.45	1.00	–	–	–	–
Lock850.083	−R	10 53 07.17	+57 28 40.0	0.22	0.19	0.26	5	0.0	−21.31	2.28	0.93	–	–	–	–
Lock850.087	RR	10 51 53.365	+57 17 30.05	2.46	2.11	2.80	7	1.6	−24.94	1.29	1.0	–	–	–	–
Lock850.100	NN	10 51 38.760	+57 15 04.70	1.37	1.28	1.56	8	0.6	−22.62	0.25	0.44	2.28	0.54	0.33	–

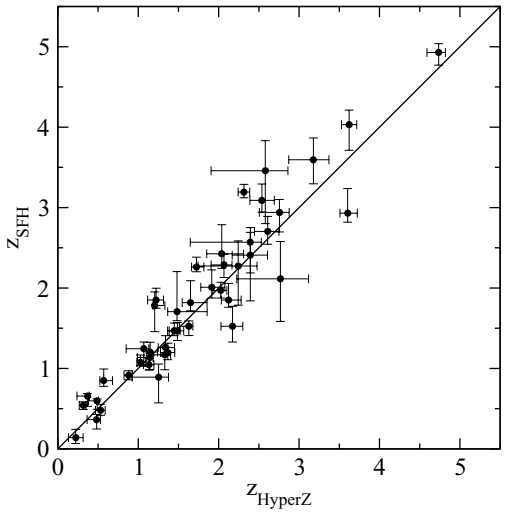

Figure 4. Comparison of the photometric redshifts computed by HYPERZ and those from the SFH analysis of Section 4.1 (1σ error bars plotted).

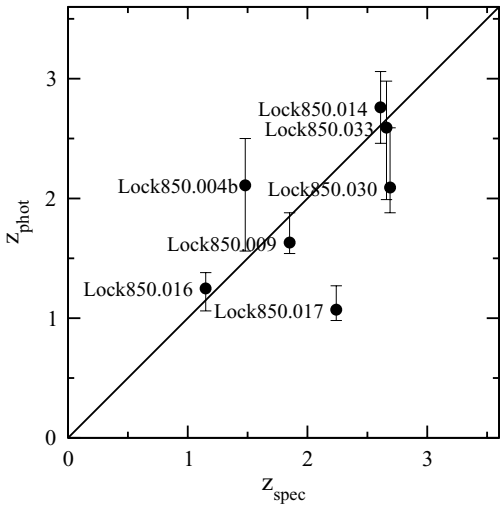

Figure 5. Comparison of photometric redshifts from this work and robust spectroscopic redshifts from Ivison et al. (2005) and Chapman et al. (2005). Error bars show the 90 per cent confidence range on the photometric redshifts.

coordinates. We determine a photometric redshift of $z = 2.22$ for the radio source and find that the photometry is well fitted by a QSO SED template. Combined with the optical morphology which exhibits arc-like structure (the arcs being a result of a relatively bright extended host galaxy), these facts suggest that Lock850.041b is very likely a strongly lensed QSO. This supports the claim of Chapman et al. (2002) that the source is a plausible lens.

Fig. 6 compares our redshifts with the photometric redshifts of Aretxaga et al. (2007) determined using the 850-μm/1.4-GHz spectral index (their '$z_{\rm phot}^{\rm MC}$'). We find a large but not significant offset between both sets of redshifts (not including sources with lower limits). Comparing the sources with $z_{\rm submm}$ derived from more than two photometric points (the filled circles in Fig. 6), our redshifts are lower by $\Delta z = 0.37 \pm 0.39$ on average, where the error here is the error on the mean. Extending this comparison to include all sources in Fig. 6, we find that our redshifts are lower by an average of $\Delta z = 0.42 \pm 0.35$ (or alternatively, as given in Table 1, the median value of $|\Delta z|$ is 0.78).

This offset manifests itself more strongly when comparing the peak of our total redshift distribution at $z \simeq 1.5$ to that of Aretxaga et al. (2007) which lies at $z \simeq 2.3$ (Chapman et al. 2005, also find that the peak of their spectroscopic redshift distribution lies at $z \simeq 2.3$). The origin of this discrepancy is not entirely clear, although the offset is reduced if the comparison is limited to the redshift distributions of only those sources plotted in Fig. 6 (i.e. those with redshifts determined by both the optical and submm/radio methods). This suggests that part of the discrepancy is a selection effect. If this is the case, then it is interesting to note how the two distributions compare to the models of van Kampen et al. (2005). A Kolmogorov–Smirnov test shows that our redshift distribution is consistent with the massive merger model whereby all SCUBA galaxies are the result of a violent merger of two galaxy sized haloes. Conversely, the redshift distribution of Aretxaga et al. (2007) is best fitted by the phenomenological model, which includes a mixture of starbursts due to mergers and quiescent star formation. Aretxaga

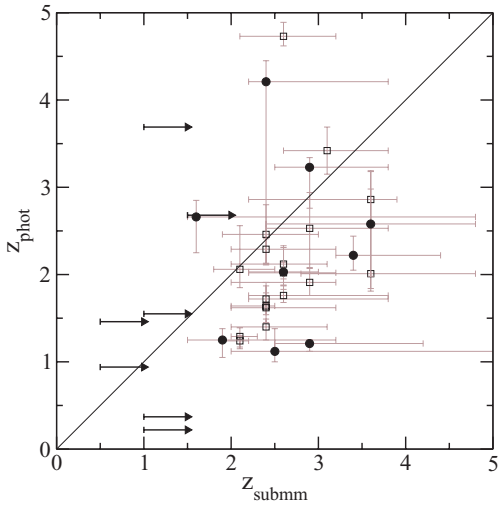

Figure 6. Comparison of photometric redshifts computed in this work ($z_{\rm phot}$) with the photometric redshifts of Aretxaga et al. (2007) derived using the 850-μm and 1.4-GHz spectral index ($z_{\rm submm}$). Open squares correspond to redshifts derived solely from 850-μm and 1.4-GHz photometry whereas filled circles correspond to redshifts derived with additional far-IR/submm photometric data. Both vertical and horizontal error bars denote the 90 per cent confidence range. The tabbed ends of the arrows show the lower limits set by Aretxaga et al. (2007).

et al. (2007) note that their redshifts are even better matched by the distribution predicted from the semi-analytical model of Silva et al. (2005) which jointly describes the formation and evolution of spheroids and QSOs. An implication of this might therefore be that SCUBA sources more readily detected in the optical are more likely to be the result of massive mergers, whereas a pure submm selected sample is more likely to include sources with quiescent star formation.

3.2.2 SED properties

Fig. A1 in Appendix A shows the best-fitting SEDs to the SHADES sources for which we have been able to estimate redshifts. The SED type and A_V given in Table 2 are plotted in Fig. 3 as a function of redshift. There are two distinct trends. First, there is a clear evolution in SED type, with late-types being found predominantly at higher redshifts and early-types at lower redshifts. Secondly, sources at $z > 2.5$ have significantly lower attenuation than sources at $z < 2.5$. Dividing the top panel of Fig. 3 by the line $A_V = 1$, it can be seen that sources at $z < 2.5$ are split equally, whereas at $z > 2.5$, 11 sources have an attenuation $A_V < 1$ with none having $A_V > 1$. We have verified that this is not a result of the way HYPERZ deals with shorter waveband dropouts by reproducing this trend independently of the configured method (see Section 3.1).

Such a decline in attenuation at high redshifts is consistent with the rate of dusty star formation having peaked at an earlier epoch (see Section 4.5), although there is a strong selection effect due to the sensitivity of the data. This decline is also reflected in the declining number of SHADES sources found beyond $z > 2.5$. This is not entirely a result of the usual selection effects since our redshifts are not subject to the optical spectroscopic redshift desert discussed in Section 1, nor are they totally reliant on there being a radio detection since the ID procedure also relies on detections at 24 μm. A similar decline in attenuation due to dust has recently been found by Buat et al. (2007). Their findings indicate a monotonic decrease in dust attenuation in luminous IR galaxies from $z = 0$ to 2 for a fixed SFR (see also Xu et al. 2007).

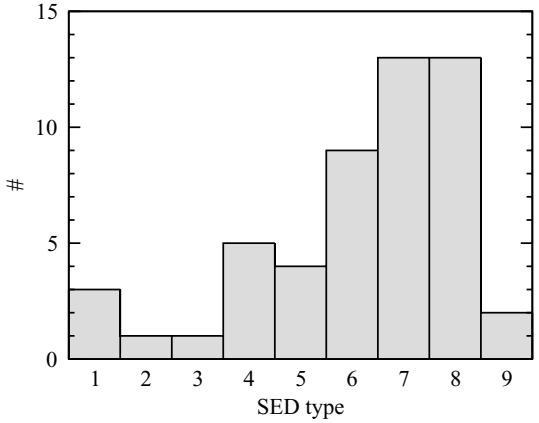

Figure 7. Histogram of best-fitting SED types for the 51 primary SHADES sources listed in Table 2. SED templates are: 1 = E, 2 = S0, 3 = Sa, 4 = Sb, 5 = Sc, 6 = Sc + Im, 7 = Im, 8 = SB, 9 = QSO.

Fig. 7 shows the distribution of SED type (listed in Table 2) for the 51 primary sources. As the figure shows, the SHADES sources are dominated by late-type SEDs. Over 80 per cent of sources have SEDs of type Sc or later and approximately two thirds of these are best fitted with either the Im or SB template. There are only two sources that are best fitted with a QSO template: Lock850.075 and Lock850.081 (there is also the secondary Lock850.041b). This is entirely consistent with the low fraction of AGN-dominated SCUBA sources found in previous studies (e.g. Ivison et al. 2002; Almaini et al. 2003; Alexander et al. 2003; Waskett et al. 2003).

4 STELLAR MASS

4.1 Method of determination

To determine stellar masses of the SHADES sources, we use the synthetic spectra of Bruzual & Charlot (2003). Rather than assume an a priori model for the SFH of each galaxy, we divide the history of each galaxy into blocks of fixed fractional time (see Section 4.2) and determine the amount of star formation in each block. We choose five blocks as a compromise; too few gives an unacceptably low SFH resolution whereas too many introduces high degeneracy between blocks and reduces the number of sources for which a stellar mass can be computed due to missing photometry. Blocks are approximately logarithmically sized to account for the fact that a galaxy's SED is more strongly influenced by more recent star formation activity.

We use the 1994 Padova stellar evolutionary tracks (Bertelli et al. 1994) with a Salpeter initial mass function (IMF) (Salpeter 1955). Starting with a simple stellar population (SSP) SED, $L_\lambda^{\rm SSP}$, we generate a composite stellar population (CSP) SED, L_λ^i, for the ith block of constant star formation in a given galaxy using

$$L_\lambda^i = \frac{1}{\Delta t_i} \int_{t_{i-1}}^{t_i} {\rm d}t' \, L_\lambda^{\rm SSP}(\tau(z) - t'), \quad (1)$$

where the block lasts from time t_{i-1} to t_i in the galaxy's history and τ is the age of the galaxy (i.e. the age of the Universe today minus the look-back time to the galaxy). The SSP SED is normalized to one solar mass hence the constant $\Delta t_i = t_i - t_{i-1}$ ensures that the

CSP is also normalized to one solar mass. We then redden the CSP SED of each block using the extinction A_V via the relationship

$$L^i_\lambda \rightarrow L^i_\lambda 10^{-0.4k(\lambda)A_V/R_V}, \quad (2)$$

where $k(\lambda)$ is given by the Calzetti law for starbursts (Calzetti et al. 2000),

$$k(\lambda) = \begin{cases} 2.659\left(-2.156 + \frac{1.509}{\lambda} - \frac{0.198}{\lambda^2} + \frac{0.011}{\lambda^3}\right) + R_V \\ \qquad (\text{for } 0.12 < \lambda < 0.63\,\mu\text{m}) \\ 2.659\left(-1.857 + \frac{1.04}{\lambda}\right) + R_V \\ \qquad (\text{for } 0.63 < \lambda < 2.2\,\mu\text{m}) \end{cases} \quad (3)$$

with $R_V = 4.05$ and λ in μm. To match our template SED coverage, we assume that the longer wavelength half of the function applies up to 10 μm, and we linearly extrapolate the shorter wavelength half down to 0.01 μm using the average slope between 0.12 and 0.13 μm.[2]

The flux (i.e. photon count) that would be observed in filter j from a given block i at the redshift z of the galaxy is

$$F_{ij} = \frac{1}{4\pi d_L^2} \int d\lambda \frac{\lambda\, L^i_\lambda(\lambda/(1+z))T_j(\lambda)}{(1+z)\,hc}, \quad (4)$$

where d_L is the luminosity distance and T_j is the transmission curve in filter j (this includes telescope and atmospheric throughput as well as detector response). We then find the normalization a_i of each block of star formation by minimizing the χ^2 function

$$\chi^2 = \sum_j^{N_{\rm filt}} \frac{\left(\sum_i^{N_{\rm block}} a_i F_{ij} - F_j^{\rm obs}\right)^2}{\sigma_j^2}, \quad (5)$$

where $F_j^{\rm obs}$ is the flux observed in filter j from the galaxy and σ_j is its error. We treat non-detections in the same way as we configured HYPERZ to, i.e. the flux is set to zero and assigned a 1σ error equal to the sensitivity of the corresponding filter.

We use a downhill simplex method to minimize χ^2. To prevent non-physical solutions we impose the constraint $a_i > 0; i = 1, N_{\rm block}$. Since the CSP SED from which F_{ij} is computed is normalized to one solar mass, the quantity a_i is the amount of stellar mass in solar units formed by the galaxy in the time interval Δt_i. The total stellar mass of the galaxy is therefore simply

$$\mathrm{M}_* = \sum_i^{N_{\rm block}} a_i. \quad (6)$$

The error on M_* is calculated by summing in quadrature the error on each a_i derived from the fit.

In minimizing χ^2 in equation (5), we have the choice of either minimizing only the quantities a_i and holding A_V and z fixed at the values determined by HYPERZ, or minimizing all parameters a_i, A_V and z. Although the latter option seems the more compelling given its self-consistency, as we show in Fig. 4, the redshifts obtained in both cases show very good agreement on the whole (see Section 3.2.1). Nevertheless, there are some significant differences and since the templates used with HYPERZ are empirical and include dust features, we choose the former option for all analysis in this paper.

[2] We have investigated the effect of different extrapolations on our results and find negligible dependence. Since the cut-off wavelength of 0.12 μm does not reach the central wavelength of our shortest filter (B band) until $z \sim 3$, this is not surprising.

4.2 Stellar mass results

We determined the stellar mass of each SHADES source using the prescription given in the preceding section. An assumption of this is that the metallicity is fixed as the source evolves. Also, the same metallicity is used for all sources. To account for these limitations, we treated the metallicity as a source of uncertainty, repeating the calculation of stellar mass for two extremes. To set this range, we used the results of Swinbank et al. (2004) who measured the metallicity of 30 high-redshift SCUBA sources. They found an approximately solar metallicity on average with a 1σ scatter of ∼0.25 dex. We therefore performed two calculations of stellar mass for each source, one using the spectra of Bruzual & Charlot (2003) with metallicity $Z = 0.4\,\mathrm{Z}_\odot$ and a second with $Z = 2.5\,\mathrm{Z}_\odot$. The resulting difference in mass was taken as the 68 per cent confidence range and combined with the Monte Carlo error as described below.

Fig. 8 shows the stellar masses computed for the SHADES sources, plotted against the rest-frame absolute K-band magnitude. The correlation is very strong with little scatter. Of the two sources best fitted with QSO templates, Lock850.081 is an outlier (as labelled) but Lock850.075 lies within the main trend with a slightly higher than median stellar mass of $3.9 \times 10^{11}\,\mathrm{M}_\odot$. The most plausible explanation for this difference is that unlike Lock850.081, the photometry of Lock850.075 is not dominated by central QSO emission. If we omit Lock850.081, linear regression gives the following relationship:

$$\log_{10} M_* = (0.59 \pm 0.05) - (0.468 \pm 0.004) M_K. \quad (7)$$

The rest-frame K-band flux is dominated by old stars and therefore, as has been appreciated for some time, provides a good mass estimator for such populations. The small scatter seen in Fig. 8 shows that rest-frame K also provides a good calibrator for the total stellar mass in SCUBA galaxies. This is a direct consequence of the fact that the average SCUBA galaxy appears to have an early and a late block of star formation which makes approximately equal amounts of old and new stars (see next section).

The average stellar mass of our sample is $10^{11.8\pm0.1}\,\mathrm{M}_\odot$. This compares favourably with an average of $10^{11.4\pm0.4}\,\mathrm{M}_\odot$ from the study of 13 SCUBA galaxies by Borys et al. (2005). Similarly, Swinbank et al. (2006) estimated dynamical masses of eight submm

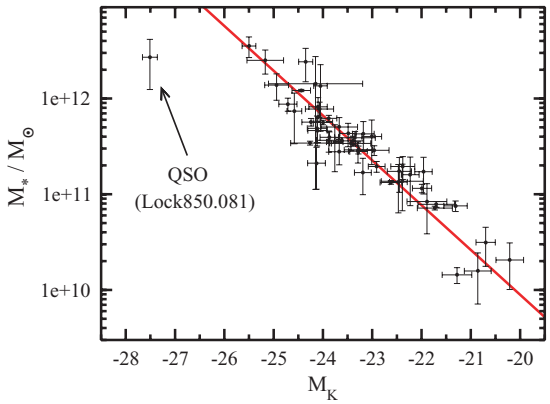

Figure 8. Variation of stellar mass of the SHADES sources with rest-frame absolute K-band magnitude (AB). Mass error bars are determined by a Monte Carlo analysis and include uncertainty due to metallicity (see text) and errors on M_K derived from redshift and photometric uncertainty. The outlying point corresponds to Lock850.081, best fitted with the QSO template. Excluding this source, the straight line fit is $\log_{10} M_* = (0.59 \pm 0.05) - (0.468 \pm 0.004) M_K$.

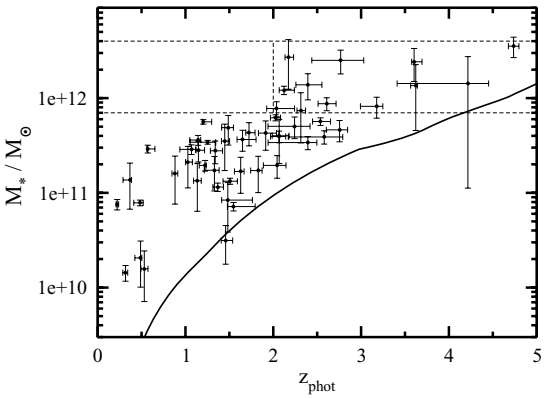

Figure 9. Variation of stellar mass of the SHADES sources with redshift. Mass error bars are determined by a Monte Carlo analysis and include uncertainty due to metallicity (see text). The continuous curve shows the mass limit transformed from the *K*-band sensitivity limit using equation (7) and our starburst SED template. The lack of objects within $7 \times 10^{11} < M_*/\mathrm{M}_\odot < 4 \times 10^{12}$ at $z < 2$ compared to the 12 objects within $2 < z < 5$ is consistent with downsizing.

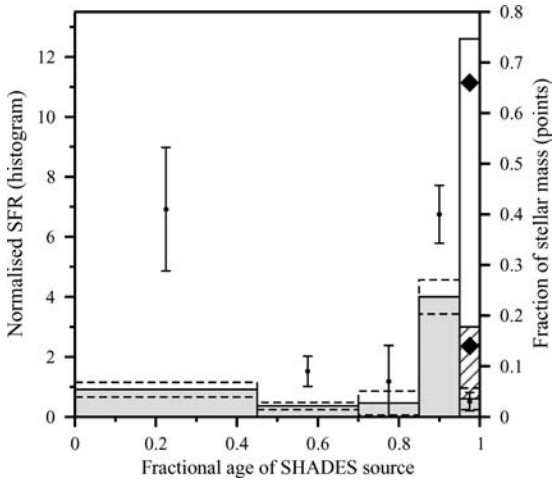

Figure 10. The normalized SFR averaged over all 51 primary SHADES sources (shaded histogram, left-hand ordinate). Upper and lower dashed histogram gives the 68 per cent confidence range allowing for uncertainty in metallicity and including the Monte Carlo scatter described in the text. The data points (right-hand ordinate) give the fraction of stellar mass created in each block on average. The last block also shows our estimate of the SFR and stellar mass created when the star formation obscured at optical/IR wavelengths is taken into account. The hatched histogram and open histogram are computed from the submm flux assuming a cold and hot SED, respectively (see Section 4.3.2). The bold rhombi give the corresponding stellar mass fractions. In this last block, both the mass fraction and SFR derived from the submm flux have been added to those derived from the optical/IR.

galaxies, finding an average of $10^{11.7\pm0.3}\,\mathrm{M}_\odot$. In terms of mass-to-light ratio (M/L), the straight line fit expressed by equation (7) gives $\mathrm{M/L} \propto L^{0.17\pm0.01}$, indicating that the mass increases more rapidly than the luminosity.

In Fig. 9, we show how stellar mass varies with photometric redshift. To obtain the mass error, we performed a Monte Carlo analysis with 1000 realizations using solar metallicity SEDs. In each realization, we computed the mass, randomly sampling the fluxes and redshift for each source using the measured errors and assuming a normal distribution. The 1σ scatter in stellar mass for each source was then added in quadrature to the 1σ error resulting from the unknown metallicity as described above. These two errors are typically approximately equal.

The continuous curve in Fig. 9 shows the mass sensitivity limit. We estimate this by firstly computing the absolute rest-frame *K*-band magnitude corresponding to the 5σ point source sensitivity of 22.9 mag (AB) at each redshift assuming our Im template SED. This is then transformed into stellar mass using the fitted relationship given in equation (7).

The horizontal dashed lines in Fig. 9 show the arbitrary selection $7 \times 10^{11} < M_*/\mathrm{M}_\odot < 4 \times 10^{12}$. These limits select the 12 most massive sources. All 12 sources lie within $2 < z < 5$. Since the comoving volume over this redshift interval is nearly twice that over $0 < z < 2$ (and since our mass sensitivity barely affects the $2 < z < 5$ selection), one would expect from simple Poisson statistics to find $\sim 6 \pm 2$ sources within $0 < z < 2$. However, there are no SHADES sources with masses greater than $7 \times 10^{11}\ \mathrm{M}_\odot$ at $z < 2$. This is evidence in favour of downsizing, whereby star formation in the Universe progressively shifts to smaller systems at later times (e.g. Cowie et al. 1996).

4.3 Star formation rate

In deriving these stellar masses, we divided the history of each galaxy into the periods (0–0.45)τ, (0.45–0.70)τ, (0.70–0.85)τ, (0.85–0.95)τ and (0.95–1)τ where τ is the age of the galaxy, taken as the age of the Universe today minus the look-back time to the source. All sources were therefore assumed to start forming immediately after the big bang.

The grey-shaded histogram in Fig. 10 shows the normalized SFR[3] in the five blocks, averaged over all 51 primary SHADES sources with photometric redshifts. As in the determination of stellar mass, the error, shown in the figure by the upper and lower dashed histograms, incorporates the uncertainty due to the unknown metallicity and the scatter from the Monte Carlo analysis. Clearly, the SFR is on average dominated by a short burst close to the epoch at which the source is observed. Since this result is derived from mainly rest-frame optical photometry, the SFR in the last block will be suppressed due to obscuration by dust. We estimate the effect of this in Section 4.3.2.

Determination of the average SFR in this way leads to a surprising result. Even though the SFR is dominated by the later stages in the average source's history, the *quantity* of stellar mass created, i.e. the area under each block in Fig. 10, is split approximately evenly between these later stages and the earliest stage (considering only the optical + IR derived results for now). Specifically, during the earliest period, 42 ± 12 per cent of the total stellar mass was formed, compared to 39 ± 6 per cent during the fourth period. In the context of our model (see below), this therefore indicates that the average SHADES source has already formed a significant fraction of its stars (also suggested by Borys et al. 2005) and that it is undergoing a second major episode of star formation at the epoch at which it is observed.

To verify the robustness of this result, we have carried out two tests. In the first test, we simply repeated the calculation twice but using two different subsets of SHADES sources. In the first subset, we selected those sources which meet the criteria $\chi^2(z) \leqslant 1.5$

[3] We define the normalized SFR as simply the fractional stellar mass formed in each block divided by the block width. Section 4.5 considers the absolute SFR.

and $p(z) \geqslant 0.9$. This leaves 27 out of the 51 primary sources with redshifts. In the second subset, we selected sources which have a robust identification in either the radio or at 24 μm or both. This gives a subset of 35 sources. The repeat calculation gives an almost identical result for both subsets, with ∼40 per cent of their stellar mass being created during the first period and ∼40 per cent being created in the fourth period.

In the second, more sophisticated test, we investigated how well our method reconstructs an input SFH. We generated three synthetic source catalogues each matching the number of SHADES sources and each made with a different average SFH. We used the Bruzual and Charlot SED library (with Salpeter IMF and $Z = Z_{\odot}$) to generate synthetic photometry in our nine wavebands. For each source, we took the redshift and A_V determined by HYPERZ and assigned photometric errors to the fluxes using a flux scaling relationship derived from the real SHADES catalogue. We then applied the analysis of Section 4.1 to assess how well the input average SFHs could be recovered.

Fig. 11 shows the results. The three panels from top to bottom, respectively, show a constant SFH, an SFH undergoing exponential decay and an SFH mimicking that exhibited by the SHADES sources. The error bars in this plot include the Monte Carlo scatter due to flux and redshift uncertainty as before. The errors are smaller than in Fig. 10 since each source is assigned exactly the same SFH, unlike the real source population which will inevitably have an intrinsic scatter. In all three cases, the reconstructed SFH very faithfully reproduces the input SFH, indicating that the trend seen in Fig. 10 is not an artefact of our method.

4.3.1 SFR evolution

We have investigated the evolution of the trend seen in the SFR by dividing the SHADES sources equally into a low- and high-redshift bin. We defined the low-redshift bin by $1 < z \leqslant 1.9$ and the high-redshift bin by $1.9 < z \leqslant 5$ (we limited this analysis to $z > 1$ since the eight sources at $z < 1$ poorly sample this large fraction of the Universe's history). Fig. 12 shows the SFHs for the two redshift bins. We also show for the final SFH block (i.e. 0.95–1 of the fractional age) our estimate of the star formation that is completely obscured by dust (Section 4.3.2). In this case, for each redshift slice, we take the average of the SFR computed from the hot and cold submm SED.

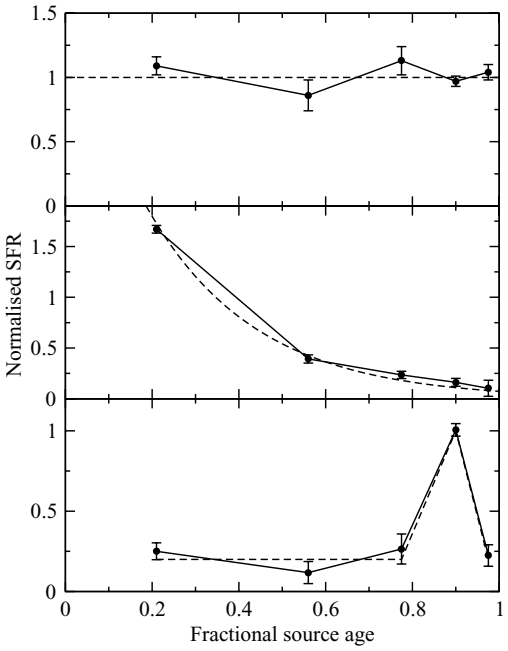

Figure 11. Input (dashed line) and reconstructed (continuous line) average SFHs. Top: Constant SFH. Middle: Exponential decay SFH. Bottom: SFH matching the average exhibited by the SHADES sources. The error bars include the Monte Carlo scatter due to flux and redshift uncertainty.

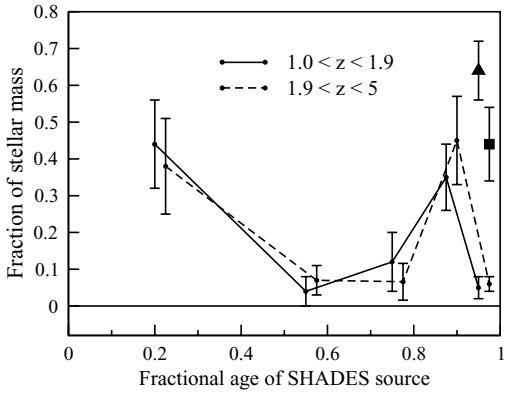

Figure 12. Average fraction of stellar mass formed as a fraction of SHADES source age for two different redshift bins (∼22 objects per bin). Data points for the lower redshift bin are offset horizontally by −0.025 for clarity. Errors account for uncertainty in metallicity and include the Monte Carlo scatter described in the text. The triangular and square points correspond, respectively, to the low- and high-redshift slices and include an estimate of the stars formed that are hidden by dust (see Section 4.3.2 – these points are averaged over the hot and cold SEDs).

Fig. 12 shows that there is little difference between the fractional formation rate of stellar mass at high and low redshifts. In both the high and low-redshift sample, the initial and late peaks in the rate of stellar mass formation persist. The late peak for the low-redshift sample is marginally less pronounced than for the high-redshift sample but still consistent within the errors. Of course, in absolute terms, the late peak in the low-redshift bin corresponds to a very different SFR to that in the high-redshift bin for two reasons. First, as Fig. 9 shows, the median mass of a SHADES source in the high-redshift bin is ∼3 times higher than the median mass in the low-redshift bin. Secondly, the proper time interval over which the late peak spans is approximately twice that for a source at $z = 1.5$ than for a source at $z = 3.5$. Therefore, on average, the late peak in the high-redshift bin corresponds to ∼5–10 times the absolute SFR of the peak in the low-redshift bin.

4.3.2 SFR: dust correction

The results presented so far are based mainly on rest-frame optical photometry. Although we have made a correction for extinction, in any system undergoing massive star formation, some of the stars are completely obscured at optical wavelengths. This is a particular problem for the SHADES sources because we observe them as a result of a massive starburst. In this section, we use the observed submm fluxes to estimate the amount of hidden star formation.

We assume that the far-IR/submm luminosity of a SHADES source is the result of a starburst extending in time over the period of the last SFH block and that this is completely hidden in the optical/near-IR wavelength range. We first calculate a pair of bolometric luminosities for each source, $L^i_{\rm hot}$ and $L^i_{\rm cold}$, using the submm flux and a hot and cold SED. These SEDs are the hottest and coolest

IRAS galaxy SEDs from the sample of Dunne & Eales (2001).[4] We then calculate the hidden SFR by taking the ratio of this luminosity and the bolometric luminosity $L^i_{\rm optical}$ for each source i of the CSP for the final block generated during the analysis of the previous section:

$$\mathrm{SFR} = \sum_i L^i_{\rm [hot,cold]} \Big/ \sum_i L^i_{\rm optical}. \quad (8)$$

This gives an upper or lower limit depending on whether the hot or cold SED is used. Since the error caused by the uncertainty in metallicity is insignificant compared to the range of SFRs spanned by the hot and cold SEDs, we ignore its contribution in this case.

The last block in Fig. 10 shows the additional hidden SFR implied by the submm flux. The hatched histogram bar is the hidden SFR assuming the cold SED and the empty histogram bar corresponds to the hot SED. Over the last 5 per cent of its history, the hidden SFR of the average SHADES source is somewhere between 6 and 30 times the SFR implied by its optical flux. Similarly, the bold rhombi show the range in the extra amount of stellar mass created in this hidden burst which is 15–65 per cent of the total stellar mass. (Note, in the figure, both the stellar mass fraction and SFR estimated from the submm have been added to the normalized quantities derived from the optical + IR.) If we therefore include the hidden star formation, somewhere between 50 per cent and 65 per cent of the stellar mass was created in the last 15 per cent of the average SHADES source's history.

4.4 The relationship of SCUBA sources to the field

Fig. 10 shows that the average SHADES source is observed during the most intense period of star formation the source has ever experienced. An interesting question is whether all galaxies endure such a phase, or whether the SHADES sources are rare in this respect. Based on the most recent two blocks in the average SHADES source's SFH, we can make the very crude statement that if all galaxies have SFHs like the average SHADES galaxy found in this study, we would expect to see somewhere between 5 per cent and 15 per cent of all galaxies undergoing a phase of highly energetic dusty star formation at any one epoch.

To test whether this is the case, we constructed a plot of the apparent I-band magnitude versus redshift for all the galaxies detected in our I-band image of the Lockman Hole. Redshifts of the field galaxies were obtained in exactly the same way as the SHADES sources using HYPERZ with the same template SEDs. We formed a master I-band catalogue using SEXTRACTOR then coincidence matched sources at all other wavelengths using a radial tolerance of 1 arcsec. We rejected stars using the CLASS_STAR parameter output by SEXTRACTOR, only retaining objects with CLASS_STAR$<$0.95 (leaving 87 per cent of objects). Objects in the vicinity of highly saturated stars were also excluded to avoid deblending problems and pixel bleeding (predominantly in the optical) as were objects detected in less than five wavebands for consistency with the SHADES sample. This leaves a total of 17 000 objects detected with 5 or more pixels above a threshold of 2σ in the full 320-arcmin^2 SHADES area.

Fig. 13 shows the $I-z$ plane for the SHADES sources (large black points) and the full field galaxies (small grey points). For comparison, the continuous curve shows the observed I-band flux of an L_* galaxy computed assuming no evolution and using our I-band filter response and Im template. The normalization of this curve is taken from Blanton et al. (2003) who measure $M_* = 5\log h - 20.82$ in I. The plot illustrates two important facts: (1) the bright envelope of full field galaxies follows the L_* galaxy track fairly closely up to and beyond the median redshift, further demonstrating that our photometric redshifts are at least reasonable, (2) the average SHADES source is significantly brighter than the average field galaxy.

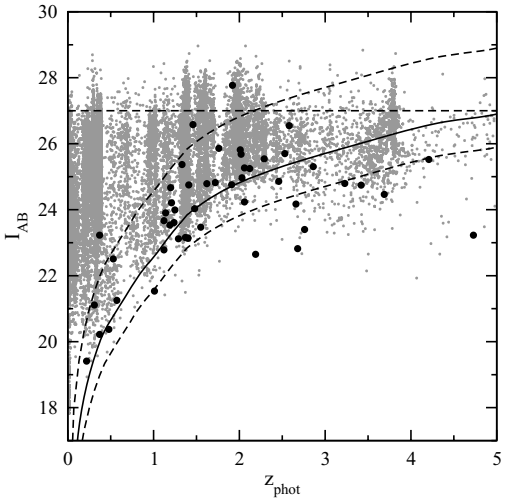

Figure 13. Apparent I-band magnitude versus redshift for the 51 primary SHADES source counterparts listed in Table 2 (black points) compared to all galaxies in the field (grey points). The continuous curve corresponds to a non-evolving L_* Im galaxy. The dashed curves are the Im track offset by $+2$ mag and -1 mag and the dashed straight line at $I_{\rm AB} = 27.0$ is the 90 per cent completeness limit.

Table 3. Evolution of the number of SHADES sources as a fraction of galaxies in the full Lockman Hole field. Both the SHADES sources and full field galaxies are selected by $L_* + 2 < L < L_* - 1$ mag and $I_{\rm AB} \leqslant 27.0$. Errors assume Poisson noise only.

Redshift	Fraction (per cent)
$0 \leqslant z < 1$	1.24 ± 0.51
$1 \leqslant z < 2$	0.72 ± 0.17
$2 \leqslant z < 3$	0.86 ± 0.26

Before the question regarding the rarity of SCUBA sources can be addressed, we must make a few further considerations. The SHADES galaxies have bright I-band magnitudes and are therefore among the most luminous galaxies at every redshift. We wish to restrict our comparison to field galaxies that are similarly luminous. We therefore limit both the SHADES and full field samples to those objects that lie within -1 and $+2$ mag of the L_* track (see Fig. 13). Secondly, we apply an upper limit of $I_{\rm AB} = 27$ where the 90 per cent completion limit takes effect. Finally, the majority of the SHADES sources are at $z < 3$ hence we limit our computation of the fraction to three redshift bins, $0 \leqslant z < 1$, $1 \leqslant z < 2$ and $2 \leqslant z < 3$.

Applying these constraints, we find in all three bins that approximately 1 per cent of galaxies in the field is a SHADES source (see Table 3). However, since we established from the average SFH that only 5–15 per cent of SHADES sources would be seen during their most active period, we can make the very approximate estimate that

[4] We choose to estimate the range of submm bolometric flux in this way for homogeneity, rather than use additional observational constraints (such as radio fluxes). The coolest SED is that of NGC 958 dominated by cold dust at 20K and the hottest is IR1525+36 with a mix of dust at 26 and 57 K in the ratio 15:1.

somewhere between one in five and one in 15 bright galaxies in the field will experience a highly energetic phase of dusty star formation. This fraction shows little evolution over $0 \leqslant z < 3$ and is consistent within the (large) errors with being constant at all redshifts in this range.

4.5 SFR density evolution

We determined the evolution of the SFR density using the 51 SHADES sources for which we were able to obtain photometric redshifts. The sources were divided into six equal redshift bins and the comoving volume density of the total SFR computed in each bin. For the SFR of each galaxy, we took the average SFR in the last two SFH blocks with and without the submm flux contribution.

The thin dashed line in Fig. 14 shows our result from the optical + IR photometry. The 68 per cent confidence range is indicated by the grey shading and accounts for the uncertainty in metallicity, the Monte Carlo scatter as in previous sections and Poisson noise. The thin continuous lines, in addition to the optical + IR photometry, include the submm flux assuming the hot and cold submm SEDs described in Section 4.3.2. The peak in both cases lies at $z \sim 2$, although the optical + IR peak is sharper than the optical + IR + submm peak, implying that the submm flux is emitted over a broader redshift interval. For comparison, we plot the SFR density measured from only submm flux by Chapman et al. (2005) and Aretxaga et al. (2007). Both of these show a peak around $2 < z < 3$ at a slightly higher redshift than our peak but not significantly so. The height of our optical + IR + submm peak is also consistent with both studies.

Compared to optical/ultraviolet (UV) observations such as the Keck Deep Field survey of Sawicki & Thompson (2006) and the Lyman break galaxy surveys of Steidel et al. (1999) and Giavalisco et al. (2004), the SFR density is ∼5–10 times lower for the SHADES sources. This suggests that at all redshifts, most of the star formation is occurring in more modest systems than the SHADES galaxies (which are at the bright end of the luminosity function). However, since the surface number density of SHADES sources in our sample is ∼100 times lower out to a redshift of $z \sim 4$ than the galaxies observed in these other surveys, the average rate of star formation per SHADES source is ∼10–20 times higher.

5 SUMMARY AND DISCUSSION

Using nine-band photometry ranging from *B* to 8 μm, we have determined best-fitting SEDs, photometric redshifts and stellar masses as well as the average SFH for 51 SCUBA sources in the Lockman Hole. We find a median redshift of $z = 1.52$ (with all objects falling in the interval $0.22 < z < 4.73$), consistent with the median photometric redshift found by Clements et al. (in preparation) for the SHADES SXDF field.

Approximately 80 per cent of sources are best fitted with late-type spectra ranging from Sc to starburst. Only two out of the 51 objects are best fitted with a QSO spectrum. Four objects are fitted with an early-type (E or S0) SED, consistent with Clements et al. (in preparation) who find two ellipticals in 33 sources. This is unexpected, especially since these four sources all have low extinction ($A_V \leqslant 0.3$). Misidentifications aside, one possibility could be that these objects have a very mixed stellar population. Young star-forming regions with a high column density of dust would be detected by SCUBA whilst being heavily obscured in the rest-frame optical. Meanwhile, old stellar regions with relatively little dust would be detected in the rest-frame optical giving the appearance of an early-type SED.

A surprising find is that the average SCUBA source has already built up a significant fraction of its stellar mass in an early period of star formation with the majority of the remainder being created in a much later and more intense burst. This is consistent with the findings of Borys et al. (2005) who concluded that the average SCUBA source already has a massive population in place by $z = 2.2$. Including 850-μm photometry indicates that a further 15–65 per cent of the total stellar mass is created in an ongoing burst of dust obscured star formation. The most recent 5–15 per cent of the average SCUBA source's history (220–660 Myr on average) shows the highest rates of star formation ever experienced by the source. Coupled with the

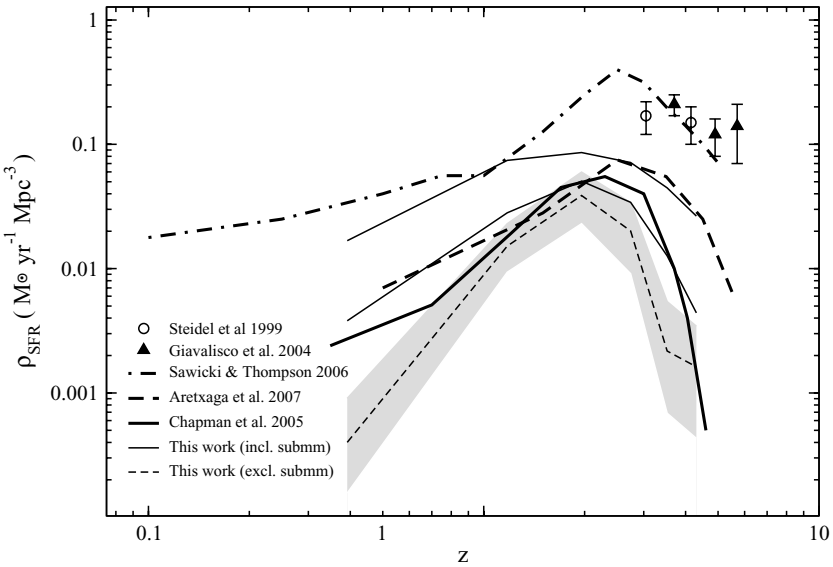

Figure 14. The SFR density of the SHADES sources. The thin dashed line is the mean density estimated from optical/near-IR photometry, with the grey shading giving the 68 per cent confidence range. The thin continuous lines show the same results but including the SFR implied from the submm flux (upper for hot SED, lower for cool SED; see Section 4.3.2). Plotted for comparison are the dust-corrected SFR densities derived from optical/UV observations of Sawiciki & Thompson (2006), Giavalisco et al. (2004) and Steidel et al. (1999). Also plotted are the SFRs determined from SCUBA galaxies by Chapman et al. (2005) (extrapolated down to 1 mJy) and Aretxaga et al. (2007) (corrected by completing the luminosity function at 60 μm).

fact that ∼1 per cent of bright field galaxies selected by $L_* + 2 < L_{\rm optical} < L_* - 1$ mag over the redshift range $0 < z < 3$ appear to be SCUBA galaxies, we estimate that between one in five and one in 15 of these galaxies will at some point in their lifetime experience a similar energetic burst of dust obscured star formation.

We find that the trend of an early and late formation of stellar mass with little intermediate activity does not differ between high ($1.9 < z < 5$) and low ($1 < z < 1.9$) redshifts. This suggests that the typical SCUBA source is a snapshot of a system at the same point in its history undergoing the same transformation process. This transformation is from a system with an already established, mature stellar population to a system with at least as much stellar mass again. This is an intriguing result and fits neatly with the conclusion of Bell et al. (2004) that the average elliptical galaxy has doubled its mass since a redshift of $z = 1$. In addition to the early and late periods of stellar mass formation, it is possible that there could also have been so-called 'dry mergers' between two systems containing old stars but little gas. In such an event, very few new stars would be formed and this therefore would not manifest itself in the SFH at the point of the merger, but would enhance the stellar mass inferred from the early source history.

There is a distinct lack of SHADES sources in the redshift interval $0 < z < 2$ with stellar masses greater than $M_* = 7 \times 10^{11}$ M$_\odot$, compared to 12 sources within $2 < z < 5$ above the same mass limit. This is clear evidence in favour of a downsizing scenario, where star formation shifts to progressively smaller systems as the Universe ages. Clements et al. (in preparation) have found exactly this trend in the SXDF.

Finally, we have determined the evolution of the SFR density using optical, IR and submm photometry. The peak occurs in the vicinity of $z \sim 2$, consistent with that determined from submm only studies (Chapman et al. 2005; Aretxaga et al. 2007) and that derived from optical/UV photometry (e.g. Sawicki & Thompson 2006). Since our sample amounts to a total of only 51 sources, we are limited by Poisson noise throughout most of the work presented here. This is especially true at $z < 1$ where we detect only eight sources. Future investigations with substantially more sensitive instruments such as SCUBA-2 and Herschel will vastly improve this shortfall.

ACKNOWLEDGMENTS

SD is supported by the Particle Physics and Astronomy Research Council. We thank Ian Smail and an anonymous referee for several helpful suggestions which have improved this manuscript. The work presented in this paper is based partly on data collected at Subaru Telescope operated by the National Astronomical Observatory of Japan, partly on data acquired by the UKIRT operated by the Joint Astronomy Centre on behalf of the UK Science and Technologies Facilities Council and partly on observations made with the *Spitzer Space Telescope* operated by the Jet Propulsion Laboratory, California Institute of Technology under a contract with NASA.

REFERENCES

Alexander D. M. et al., 2003, AJ, 125, 383
Almaini O. et al., 2003, MNRAS, 338, 303
Aretxaga I. et al., 2007, MNRAS, 379, 1571
Barger A. J., Cowie L. L., Sanders D. B., Fulton E., Taniguchi Y., Sato Y., Kawara K., Okuda H., 1998, Nat, 394, 248
Bell E. F. et al., 2004, ApJ, 608, 752
Benitez N., 2000, ApJ, 536, 571
Bertelli G., Bressan A., Bertelli G., Chiosi C., Fagotto F., Nasi E., 1994, A&AS, 106, 275
Bertin E., Arnouts S., 1996, A&AS, 117, 393
Blain A. W., Chapman S. C., Smail I., Ivison R., 2004, ApJ, 611, 725
Blanton M. R. et al., 2003, ApJ, 592, 819
Bolzonella M., Miralles J.-M., Pelló R., 2000, A&A 363, 476
Borys C., Smail, Ian, Chapman S. C., Blain A. W., Alexander D. M., Ivison R. J., 2005, ApJ, 2005, 635, 853
Brotherton M. S., Tran H. D., Becker R. H., Gregg M. D., Laurent-Muehleisen S. A., White R. L., 2001, ApJ, 546, 775
Bruzual G., Charlot S., 2003, MNRAS, 344, 1000
Buat V., Marcillac D., Burgarella D., Le Floc'h E., Rieke G., Takeuchi T. T., Iglesias-Paramo J., Xu C. K., 2007, A&A, 469, 19
Calzetti D., Armus L., Bohlin R. C., Kinney A. L., Koorneef J., Storchi-Bermann T., 2000, ApJ, 533, 682
Chapman S. C., Smail I., Ivison R. J., Blain A. W., 2002, MNRAS, 335, L17
Chapman S. C., Blain A. W., Smail I., Ivison R. J., 2005, ApJ, 622, 772
Coleman G. D., Wu C.-C., Weedman D. W., 1980, ApJS, 43, 393
Coppin K. et al., 2006, MNRAS, 372, 1621
Coppin K. et al., 2008, MNRAS, 384, 1597
Cowie L. L., Songaila A., Hu E. M., Cohen J. G., 1996, AJ, 112, 839
Downes A. J. B., Peacock J. A., Savage A., Carrie D. R., 1986, MNRAS, 218, 31
Dunne L., Eales S. A., Edmunds M. G., 2003, MNRAS, 341, 589
Dunne L., Eales S. A., 2001, MNRAS, 327, 697
Dye S. et al., 2006, MNRAS, 372, 1227
Egami E. et al., 2004, ApJS, 154, 130
Elvis M. et al., 1994, ApJS, 95, 1
Eyles L. P., Bunker A. J., Ellis R. S., Lacy M., Stanway E. R., Stark D. P., Chiu K., 2007, MNRAS, 374, 910
Fazio G. G. et al., 2004, ApJS, 154, 10
Gordon K. D. et al., 2005, PASP, 117, 503
Giavalisco M. et al., 2004, ApJ, 600, L103
Holland W. S. et al., 1999, 303, 659
Huang J.-S. et al., 2004, ApJS, 154, 44
Hughes D. H. et al., 1998, Nat, 394, 241
Ivison R. J. et al., 2002, MNRAS, 337, 1
Ivison R. J. et al., 2004, ApJS, 154, 124
Ivison R. J. et al., 2005, MNRAS, 364, 1025
Ivison R. J. et al., 2007, MNRAS, 380, 199
Kinney A. L., Calzetti D., Bohlin R. C., McQuade K., Storchi-Bergmann T., Schmitt H. R., 1996, ApJ, 467, 38
Lawrence A. et al., 2007, MNRAS, 379, 1599
Lu N. et al., 2003, ApJ, 588, 199
Mannucci E., Basile F., Poggianti B. M., Cimatti A., Daddi E., Pozzetti L., Vanzi L., 2001, MNRAS, 326, 745
Miyazaki S. et al., 2002, PASJ, 54, 833
Mortier A. et al., 2005, MNRAS, 363, 563
Rieke G. et al., 2004, ApJS, 154, 25
Salpeter E. E., 1955, ApJ, 121, 161
Sawicki M., Thompson D., 2006, ApJ, 648, 299
Scott S. E. et al., 2002, MNRAS, 331, 817
Silva L., De Zotti G., Granato G. L., Maiolino R., Danese L., 2005, MNRAS, 357, 1295
Smail I., Ivison R. J., Blain A. W., 1997, ApJ, 490, L5
Steidel C. C. et al., 1999, ApJ, 519, 1
Swinbank A. M., Smail I., Chapman S. C., Blain A. W., Ivison R. J., Keel W. C., 2004, ApJ, 617, 64
Swinbank A. M., Chapman S. C., Smail I., Lindner C., Borys C., Blain A. W., Ivison R. J., Lewis G. F., 2006, MNRAS, 371, 465
Takagi T. et al., 2007, MNRAS, 381, 1154
van Kampen E. et al., 2005, MNRAS, 359, 469
Warren S. J. et al., 2007, MNRAS, 375, 213
Waskett T. et al., 2003, MNRAS, 341, 1217
Xu C. K., 2007, ApJS, 173, 432

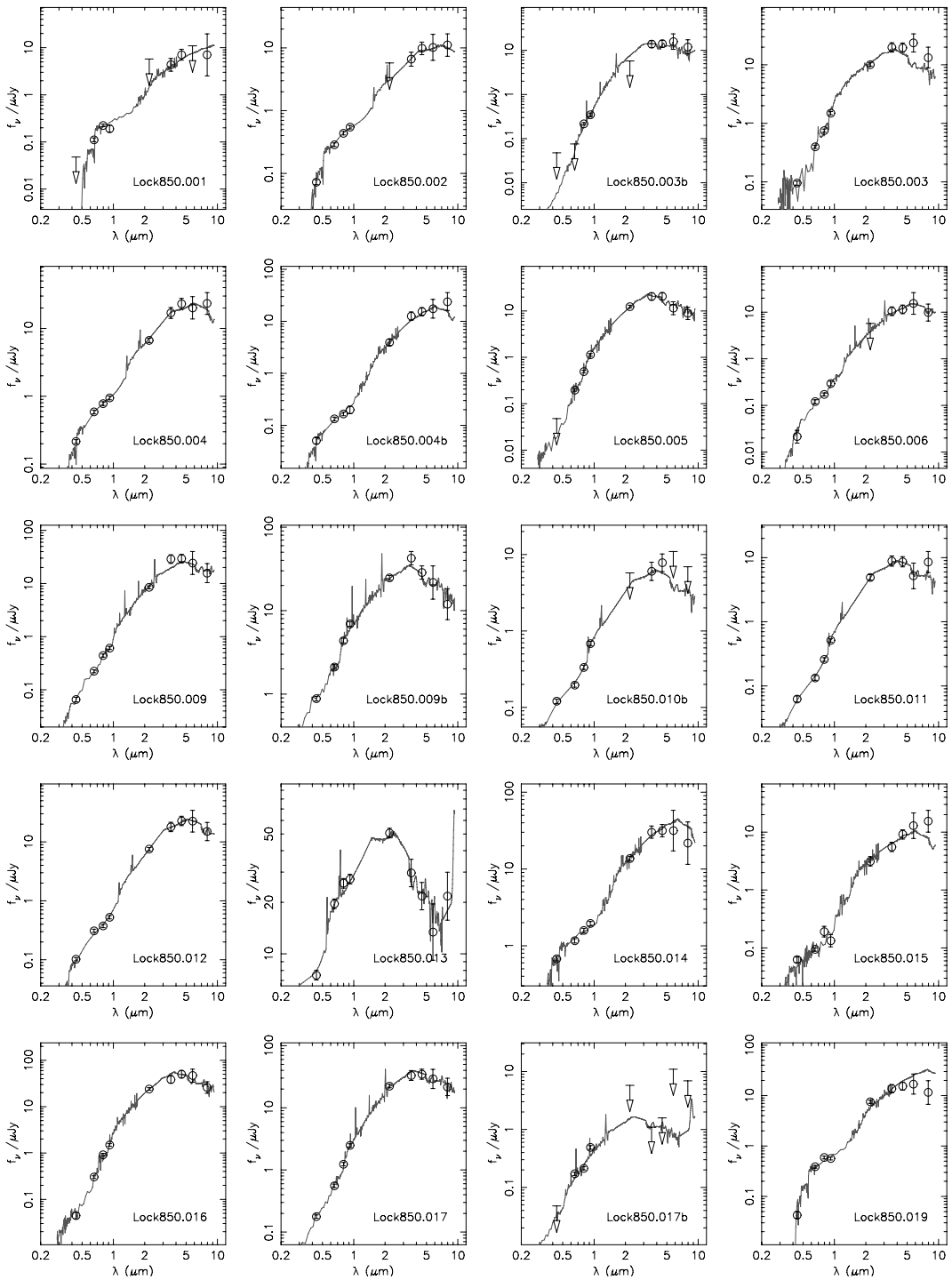

Figure A1. Best-fitting SEDs for the SHADES sources determined by HYPERZ. Photometric points plot 1 σ error bars. Table 2 lists photometric redshifts, SED type, A_V and absolute K-band magnitude for each source.

APPENDIX A: SED PLOTS AND POSTAGE STAMPS

Fig. A1 plots the best-fitting template SEDs to the SHADES sources with redshifts listed in Table 2.

Postage stamp images for all wavelengths are illustrated in Fig. A2.

APPENDIX B: NOTES ON SOURCES

In this appendix, we provide descriptions for a selection of noteworthy sources.

Lock850.001: This is a distinct source detected in *RIz* and all IRAC bands apart from 5.8 μm. There is an unambiguous detection at

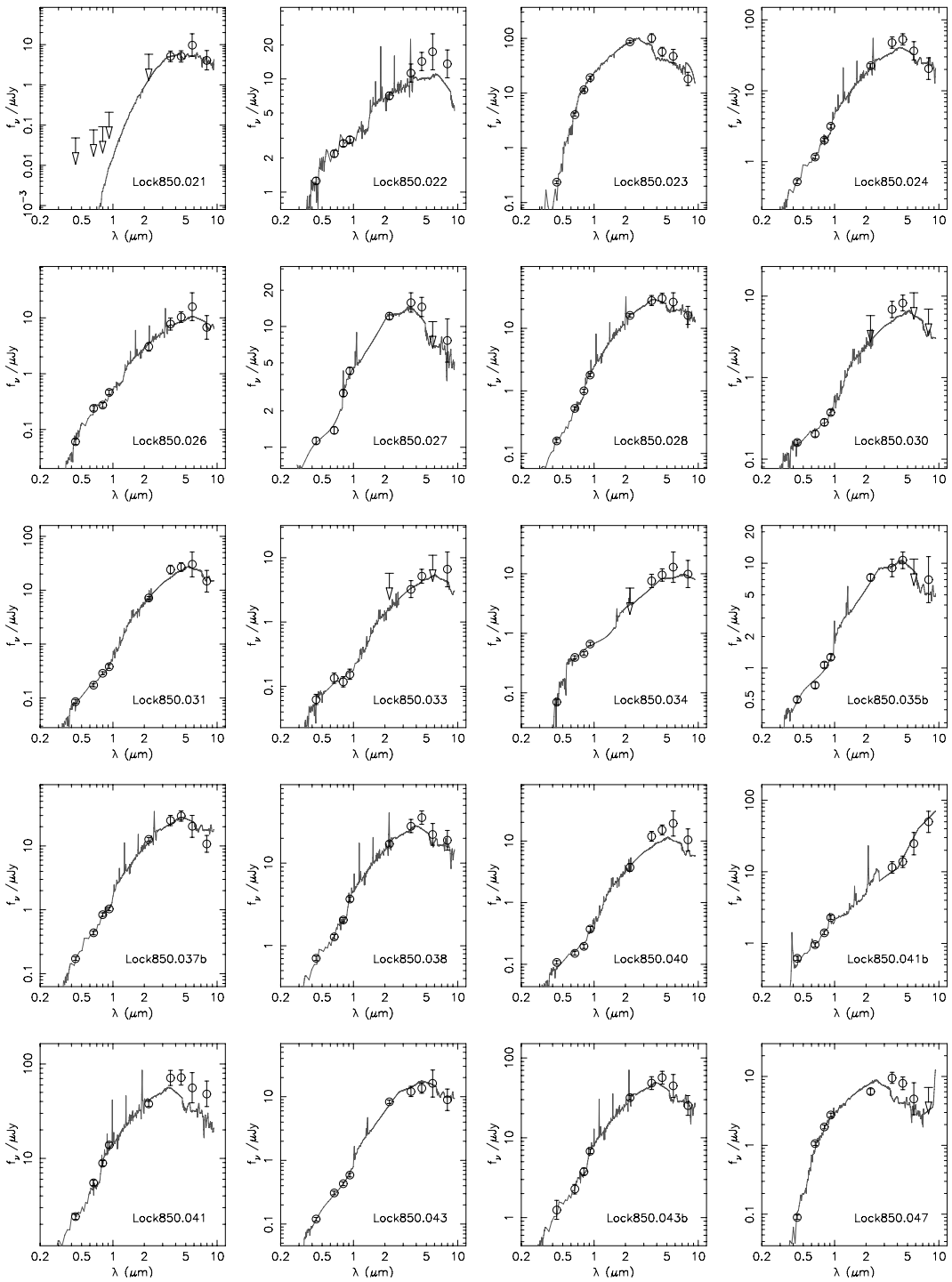

Figure A1 – *continued*

24 μm and 1.4 GHz. The source is probably blended with a fainter neighbour to the west in the 3.6- and 4.5-μm data. The SED and redshift are derived from deblended photometry but using blended photometry makes little difference to the resulting SED and redshift of $z = 4.2$.

Lock850.003: There are two highly likely counterparts to this source, both with robust radio and 24-μm detections. The primary is the fainter but more probable in both the radio and at 24 μm with an offset of ∼1 arcsec from the SCUBA position compared to ∼3 arcsec of the secondary. The two counterparts have consistent photometric redshifts of $z = 1.21^{+0.04}_{-0.09}$ and $z = 1.51^{+0.10}_{-0.27}$. These are inconsistent with the spectroscopic redshift of $z = 3.04$ deemed non-robust by Ivison et al. (2005).

Lock850.004: There are two robust counterparts, both with significant detections at all wavelengths, in particular at 24 μm and 1.4 GHz. The primary counterpart has the lowest P in both the

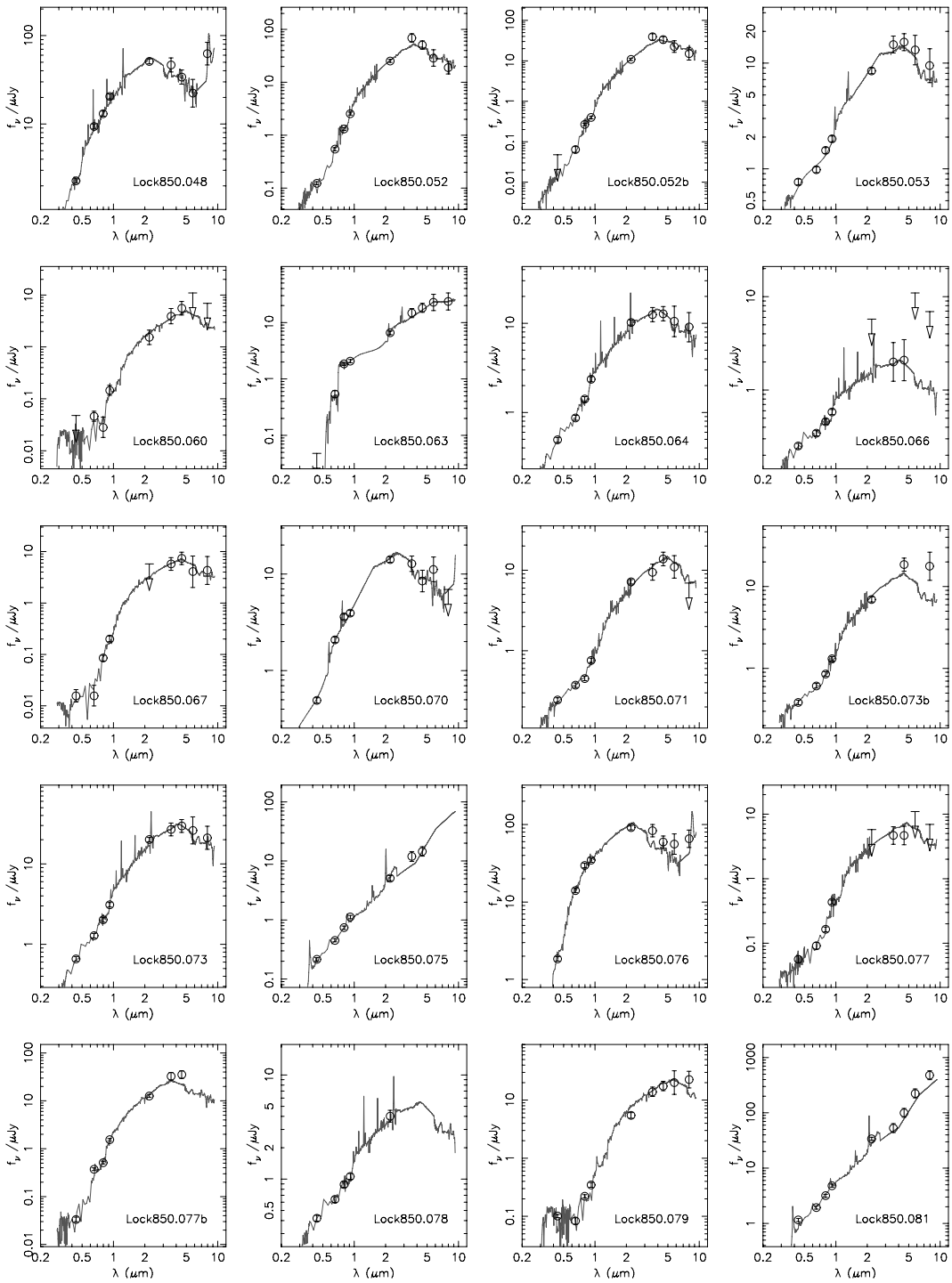

Figure A1 – *continued*

radio and at 24 μm. The spectroscopic redshift for the primary is considered non-robust. A third source lying ∼9 arcsec to the north–north-west is brighter than the primary in the radio and at 24 μm and has a photometric redshift of $z = 3.0$ with an early-type SED.

Lock850.005: The most likely counterpart is a faint non-robust 24-μm source lying ∼5 arcsec from the SCUBA position in a south–south-east direction. There are no radio counterparts detected for this source.

Lock850.007: There is a single robust radio and 24-μm counterpart but all wavebands show strong blending with a bright neighbour which cannot be reliably deblended. This source is therefore omitted from the photometric redshift analysis.

Lock850.008: Optical photometry of this source is affected by pixel bleeding from a nearby bright star and at IRAC wavelengths, the source is blended with a neighbour of comparable brightness. The source is therefore omitted from the photometric redshift analysis.

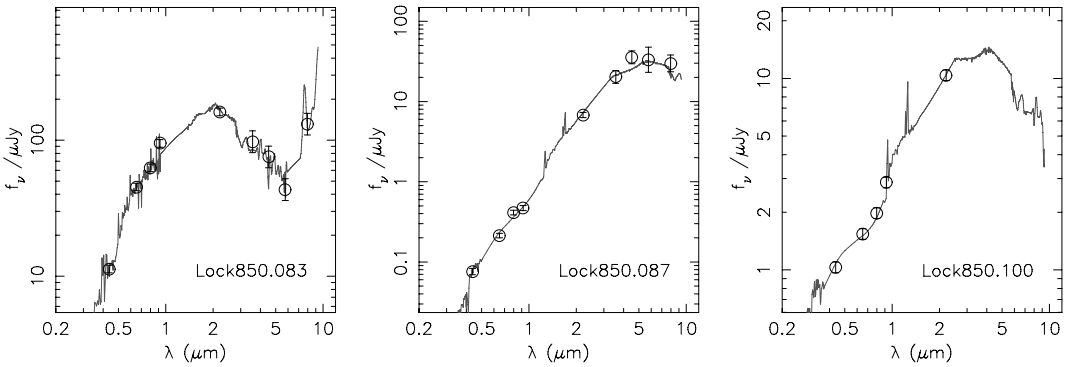

Figure A1 – *continued*

Lock850.009: The primary counterpart is the only robust radio source and the most likely robust 24-μm source. The secondary counterpart included in Table 2 has a robust 24-μm detection ($P = 0.043$) offset 3.8 arcsec from the SCUBA position but is not detected in the radio.

Lock850.010: The robust radio counterpart reported in Ivison et al. (2007) is only detected in the first two IRAC bands, hence no photometric redshift can be determined for this source. The secondary counterpart in Table 2 is the most likely 24-μm counterpart, is detected at all wavelengths (apart from the radio), has an offset of ∼8 arcsec south–south-west from the SCUBA position and is not robust with $P = 0.31$.

Lock850.011: There are no robust radio or 24-μm counterparts for this source. The most likely counterpart is not detected in the radio but is detected at 24 μm with a near-robust $P = 0.053$.

Lock850.015: This source has two robust radio counterparts, both close to each other (∼2 arcsec) and close to the SCUBA position (both offset by ∼2 arcsec). The primary counterpart is brighter in the radio than the secondary and is the only source of the two to be detected at 24 μm. The secondary is included in Table 2 by virtue of having a robust radio detection but is not detected at any other wavelength and hence has an undetermined photometric redshift.

Lock850.017: At optical wavelengths, the primary counterpart to this source has a morphology comprising a centrally bright compact nucleus and a more diffuse tail extending to the south-west. An explanation for the discrepancy between the photometric and spectroscopic redshifts may be that the tail is a separate background object; the photometry is dominated by flux from the compact object whereas emission lines seen in the spectra may originate from the diffuse object in the background. The secondary counterpart with a robust 24-μm detection listed in Table 2 is offset ∼2 arcsec due east, is very faint at all wavelengths and is best fitted with the SB template but with an unacceptable χ^2.

Lock850.021: No radio counterparts are detected for this source. The only robust 24-μm detection is taken as the primary counterpart but this is only detected in the four IRAC wavebands. The only other 24-μm source detected within 15 arcsec of the SCUBA position is non-robust, has an offset of ∼6 arcsec south-west, is brighter than the primary at all wavelengths and has a photometric redshift of $z = 1.4$ with an Im type SED.

Lock850.023: Ivison et al. (2007) report two non-robust 24-μm counterparts with approximately equal values of P. There are no radio sources detected. The slightly more probable (numerically lower P) 24-μm source is taken as the primary counterpart and has a very faint 24-μm flux and an SED that corresponds to a $z \simeq 0.1$ elliptical (consistent with its optical morphology). The less probable 24-μm source has a stronger 24-μm flux and photometry consistent with a starburst at $z \simeq 2.7$.

Lock850.027: The primary counterpart has no radio detection but a non-robust faint 24-μm detection (106 ± 15 μJy) offset ∼6 arcsec to the north from the SCUBA position, consistent with an Im galaxy at $z = 1.1$. Another possible counterpart, not listed in Table 2 since it is offset ∼11 arcsec to the south-east, has a faint non-robust 1.4-GHz detection and a brighter but still non-robust 24-μm detection (196 ± 13 μJy). The optical morphology and photometry of this source are consistent with an S0 galaxy at $z \simeq 0.6$.

Lock850.029: No counterpart is detected at the position of the most likely radio source noted by Ivison et al. (2007) at any other wavelength. Another source lies ∼8 arcsec north-west from the SCUBA position and is detected at 24 μm with $P = 0.15$. This source is detected with high S/N at all wavelengths, particularly at IRAC wavelengths (but is not detected in the radio) and has photometry consistent with a Sa galaxy at $z = 1.4$.

Lock850.030: This counterpart has strong radio and 24-μm flux and lies ∼3 arcsec to the south-west of the SCUBA position. It is faint but unambiguous at almost all other wavelengths, giving rise to a relatively uncertain photometric redshift, marginally consistent with the measured spectroscopic redshift.

Lock850.035: The most probable counterpart to this source reported by Ivison et al. (2007) is a non-robust radio source with a probability $P = 0.065$ offset to the south-west by ∼5 arcsec from the SCUBA position. This source is not detected at any other wavelength, therefore we include a secondary counterpart in Table 2 as an alternative possibility, this object having the most probable 24-μm detection seen at other wavelengths. This secondary counterpart is offset by ∼9 arcsec south-west of the SCUBA position, has irregular optical morphology and is well fitted by an Im SED at $z = 1.6$.

Lock850.036: No radio or 24-μm counterpart detected for this source. Directly east at an offset of ∼8 arcsec from the SCUBA position lies an irregular object which shows bright emission at

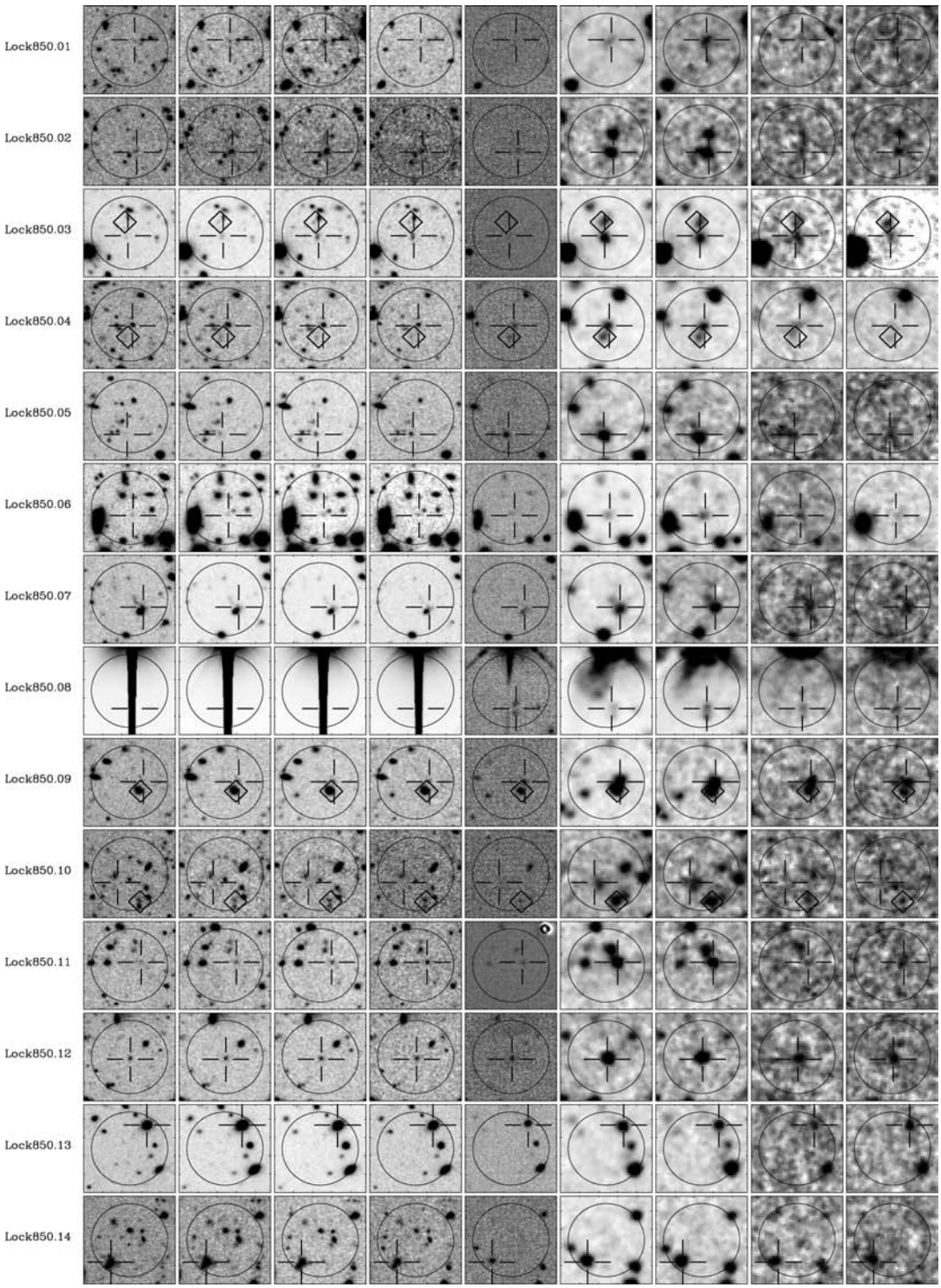

Figure A2. Postage stamp images (24 × 24 arcsec^2) for all 60 SHADES sources. Columns from left- to right-hand side correspond to: *B*, *R*, *I*, *z*, *K*, 3.6, 4.5, 5.8 and 8 μm. The cross-hair shows the location of the primary counterpart and the diamond, where present, shows the secondary. The 10 arcsec radius circle is centred on the SCUBA position.

IRAC wavelengths. Surprisingly, the photometry of this source is well fitted by an elliptical SED with a redshift of $z = 0.9$.

Lock850.037: The most probable counterpart reported by Ivison et al. (2007) is detected only in the radio. Table 2 includes a secondary counterpart with a robust 24-μm detection and a non-robust radio detection lying ∼6 arcsec south-east from the SCUBA position. The secondary is the only source detected within 10 arcsec at 5.8 and 8 μm and the brightest of two at 24 μm.

Lock850.041: There are two very likely counterparts, both with robust detections at 24 μm and in the radio. Both have a high S/N at

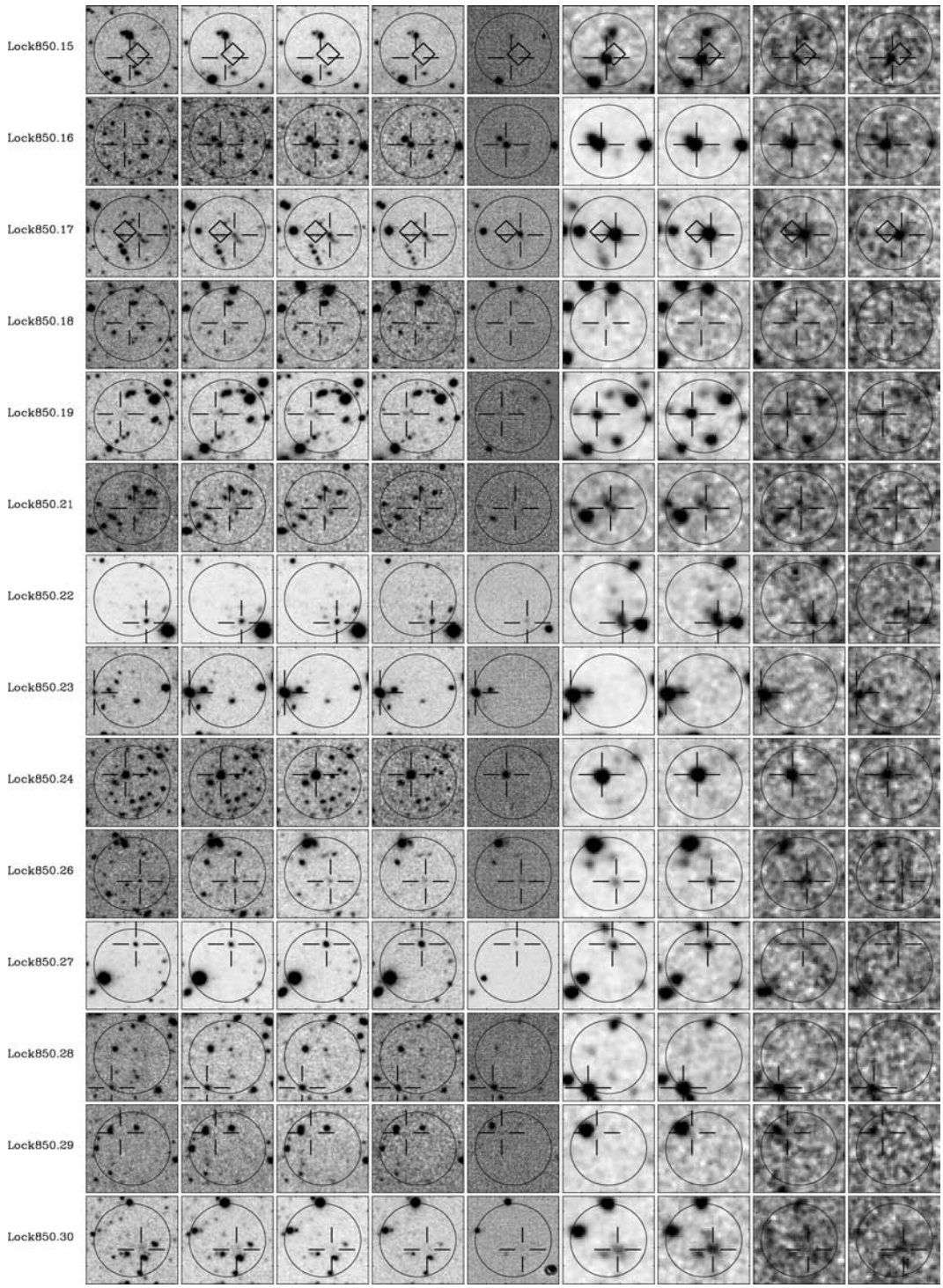

Figure A2 – *continued*

all wavelengths. The most likely counterpart has photometry consistent with a $z \sim 1$ starburst, whereas the slightly less favourable counterpart (Lock850.041b) is very well fitted by a QSO template. As explained in the text (see Section 3.2.1), Lock850.041b is most likely a $z \simeq 2.2$ QSO strongly magnified by a $z = 0.7$ (Ivison et al. 2005) elliptical lens 2 arcsec to the south-west.

Lock850.043: There are two robust 24-μm counterparts detected at all wavelengths for this source. The primary is the nearer of the two with a lower P value and offset west by ∼5 arcsec from the SCUBA position. The counterpart has a significant but not quite robust radio detection and a weaker 24-μm flux. The secondary counterpart is slightly blended in B with two neighbours lying to the

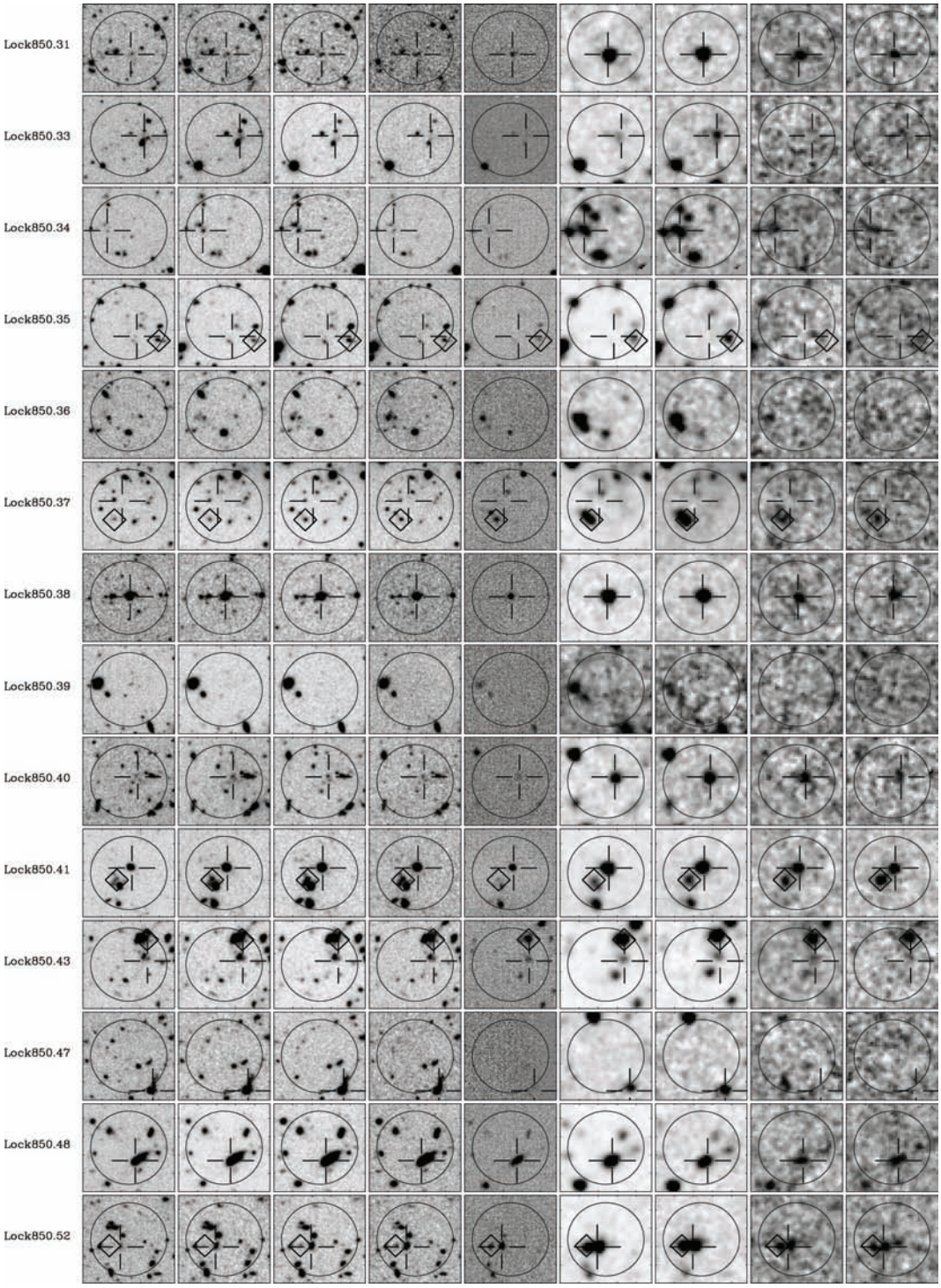

Figure A2 – *continued*

east, becoming less blended at longer wavelengths where it becomes dominant. The secondary counterpart lies ∼8 arcsec north-west of the SCUBA position, has a stronger 24-μm flux but a very similar photometric redshift of $z = 1.20$.

Lock850.047: The counterpart for this source has a very disturbed optical morphology with a long (∼4 arcsec) 'tail' extending north–north-east. The radio and 24-μm position are both located at the same point in the 'tail'. The photometry was measured in an aperture centred on the radio position and is probably contaminated by the brighter more compact source from which the tail appears to emanate. This most likely causes the poor SED fit and hence uncertain photometric redshift of $z = 0.4$.

Lock850.052: Both primary and secondary counterparts have consistent photometric redshifts ($z \simeq 1.2$) and both are very well fitted

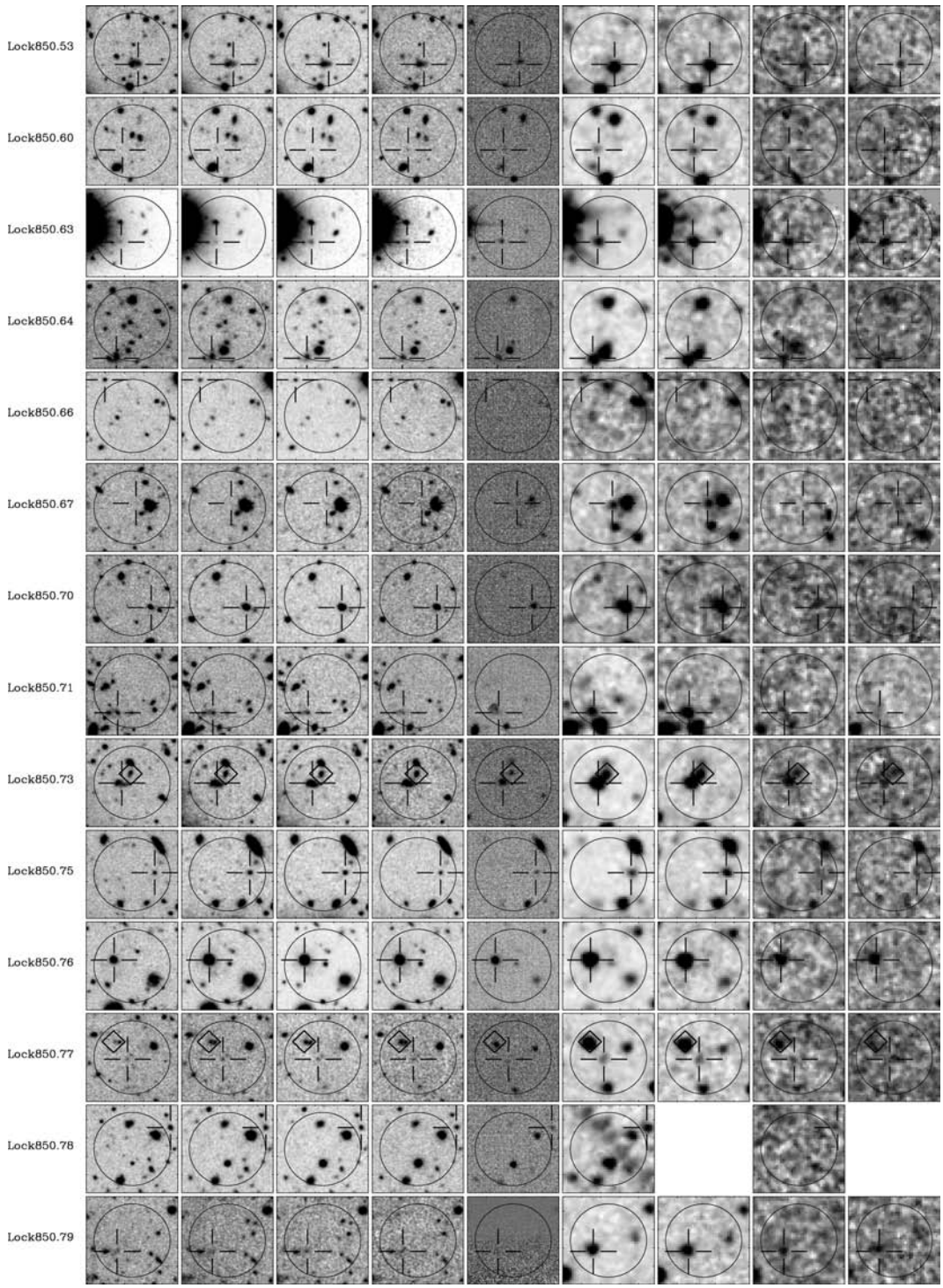

Figure A2 – *continued*

with similar SED types (Sb/Sc). The primary, offset ∼3 arcsec east–south-east from the SCUBA position, has a robust radio and 24-μm detection, whereas the secondary, offset ∼5 arcsec east–south-east has a robust 24-μm detection but no radio detection.

Lock850.064: There are three bright sources detected at IRAC wavelengths within 10 arcsec of the SCUBA position. The primary counterpart is the only one with significant 24-μm flux although it is non-robust being offset by nearly 10 arcsec to the south–south-east. The source is detected in the radio (also non-robust) and is mildly blended with a neighbour of similar brightness at IRAC wavelengths.

Lock850.073: The primary and secondary counterparts have consistent photometric redshifts and are well fitted by late-type SEDs. The primary shows an irregular optical morphology and has robust

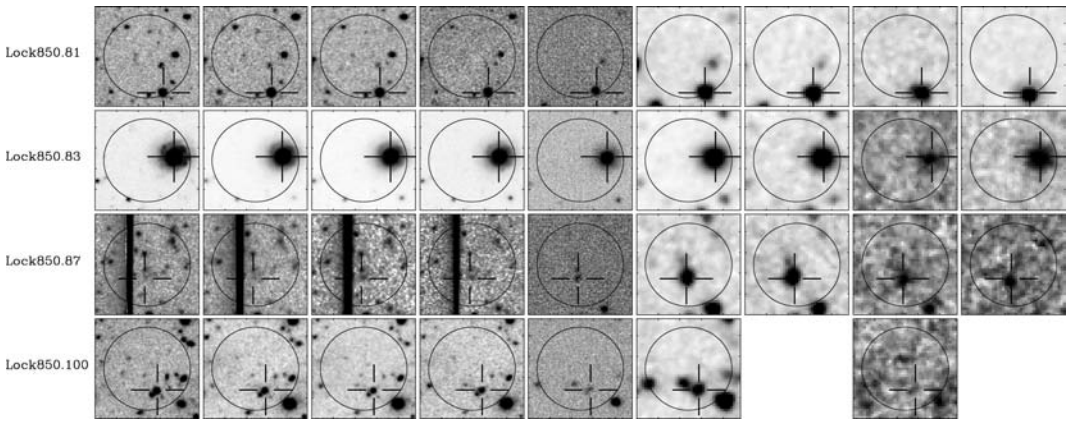

Figure A2 – *continued*

radio and 24-μm detections. The secondary has a similar offset to the primary from the SCUBA position (∼2.6 arcsec), has a robust radio detection but is not detected at 24 μm.

Lock850.077: This source has two possible counterparts. The primary gains its status by virtue of being close to the SCUBA position (∼1.5 arcsec to the east) thereby having robust radio and 24-μm detections. The brighter secondary (three times the flux in the radio and at 24 μm) is offset approximately 6 arcsec to the east–north-east of the SCUBA position and the optical morphology clearly shows two very close (< 1 arcsec) objects of equal flux and size. The 3-arcsec aperture we use completely encompasses both of these objects belonging to the secondary and therefore inaccurate deblending may explain the very poor SED fit.

Lock850.083: The only plausible counterpart for this source is a nearby spiral galaxy with a photometric redshift of $z = 0.22$ offset ∼8 arcsec west of the SCUBA position. The source has a robust 24-μm detection but is not detected in the radio. This object is best fitted with a type Sc SED, perfectly consistent with its optical morphology.

Lock850.100: There are two very close potential counterparts for this source. The primary counterpart is the brighter of the two, with a photometric redshift of $z = 1.4$ and having photometry consistent with a starburst galaxy. The fainter source is best fitted with an Im SED at $z = 0.4$. The IRAC photometry is omitted for this object as the primary counterpart cannot be deblended with its neighbour due to the IRAC PSF.

APPENDIX C: PHOTOMETRIC DATA

Table C1 lists the optical to mid-IR photometry for all SHADES source counterparts discussed in this paper. All magnitudes are in the AB system and were extracted using an effective 3 arcsec diameter aperture (see Section 2 for more details). All photometric errors were combined in quadrature with an error of 0.05 to account for uncertainties in zero-point.

Table C1. The optical to mid-IR photometry for all SHADES source counterparts. Magnitudes are in the AB system and correspond to an effective 3 arcsec diameter aperture (see Section 2). A numerical value of 99 corresponds to a non-detection, whereas a dash (–) indicates that photometry could not be extracted. Errors include the zero-point uncertainty in each waveband.

ID	*B*	*R*	*I*	*z*	*K*	3.6 μm	4.5 μm	5.8 μm	8 μm
Lock850.001	99	26.29 ± 0.10	25.52 ± 0.07	25.70 ± 0.18	99	22.31 ± 0.34	21.77 ± 0.29	99	21.78 ± 1.12
Lock850.002	26.75 ± 0.10	25.26 ± 0.06	24.80 ± 0.06	24.56 ± 0.07	99	21.85 ± 0.28	21.42 ± 0.25	21.38 ± 0.52	21.29 ± 0.45
Lock850.003	26.45 ± 0.09	24.90 ± 0.06	24.21 ± 0.06	23.47 ± 0.06	21.39 ± 0.06	20.66 ± 0.21	20.67 ± 0.20	20.47 ± 0.39	21.09 ± 0.44
Lock850.003b	99	99	25.56 ± 0.07	25.05 ± 0.10	99	21.05 ± 0.19	21.03 ± 0.21	20.90 ± 0.44	21.20 ± 0.40
Lock850.004	25.57 ± 0.06	24.48 ± 0.06	24.17 ± 0.06	23.96 ± 0.06	21.84 ± 0.08	20.83 ± 0.20	20.49 ± 0.19	20.64 ± 0.41	20.48 ± 0.40
Lock850.004b	27.14 ± 0.15	26.09 ± 0.09	25.85 ± 0.09	25.66 ± 0.18	22.41 ± 0.15	21.15 ± 0.19	20.94 ± 0.18	20.79 ± 0.45	20.45 ± 0.43
Lock850.005	99	25.66 ± 0.06	24.67 ± 0.06	23.77 ± 0.06	21.16 ± 0.06	20.62 ± 0.20	20.61 ± 0.21	21.25 ± 0.35	21.53 ± 0.33
Lock850.006	28.08 ± 0.34	26.20 ± 0.10	25.81 ± 0.08	25.22 ± 0.12	99	21.35 ± 0.23	21.25 ± 0.23	20.93 ± 0.58	21.42 ± 0.46
Lock850.007	–	–	–	–	–	–	–	–	–
Lock850.008	–	–	–	–	–	–	–	–	–
Lock850.009	26.86 ± 0.11	25.53 ± 0.06	24.79 ± 0.06	24.43 ± 0.06	21.58 ± 0.06	20.25 ± 0.20	20.23 ± 0.22	20.43 ± 0.54	20.91 ± 0.45
Lock850.009b	24.04 ± 0.06	23.09 ± 0.06	22.30 ± 0.06	21.80 ± 0.06	20.42 ± 0.06	19.83 ± 0.19	20.26 ± 0.16	20.56 ± 0.50	21.21 ± 0.46
Lock850.010	99	99	99	99	99	22.71 ± 0.40	22.27 ± 0.35	99	99
Lock850.010b	26.20 ± 0.06	25.67 ± 0.06	25.09 ± 0.06	24.31 ± 0.06	99	21.95 ± 0.30	21.67 ± 0.29	99	99
Lock850.011	26.91 ± 0.12	26.09 ± 0.09	25.37 ± 0.06	24.63 ± 0.07	22.17 ± 0.11	21.53 ± 0.19	21.56 ± 0.18	22.11 ± 0.50	21.57 ± 0.41
Lock850.012	26.38 ± 0.07	25.17 ± 0.06	24.97 ± 0.06	24.60 ± 0.07	21.71 ± 0.07	20.77 ± 0.20	20.51 ± 0.18	20.52 ± 0.46	20.96 ± 0.39
Lock850.013	21.71 ± 0.06	20.67 ± 0.06	20.37 ± 0.06	20.31 ± 0.06	19.64 ± 0.06	20.22 ± 0.20	20.56 ± 0.16	21.08 ± 0.41	20.56 ± 0.35
Lock850.014	24.32 ± 0.06	23.74 ± 0.06	23.40 ± 0.06	23.18 ± 0.06	21.06 ± 0.06	20.20 ± 0.19	20.15 ± 0.21	20.15 ± 0.66	20.56 ± 0.69
Lock850.015	26.91 ± 0.12	26.47 ± 0.07	25.70 ± 0.23	26.09 ± 0.26	22.66 ± 0.20	22.04 ± 0.20	21.50 ± 0.20	21.12 ± 0.55	20.93 ± 0.47
Lock850.015b	99	99	99	99	99	21.47 ± 0.25	20.98 ± 0.21	99	99

Table C1 – *continued*

ID	*B*	*R*	*I*	*z*	*K*	3.6 μm	4.5 μm	5.8 μm	8 μm
Lock850.016	27.28 ± 0.17	25.20 ± 0.06	23.99 ± 0.06	23.47 ± 0.06	20.45 ± 0.06	19.93 ± 0.21	19.65 ± 0.22	19.73 ± 0.35	20.37 ± 0.31
Lock850.017	25.78 ± 0.06	24.54 ± 0.06	23.67 ± 0.06	22.92 ± 0.06	20.53 ± 0.06	20.10 ± 0.20	20.05 ± 0.18	20.24 ± 0.39	20.56 ± 0.35
Lock850.017b	99	25.82 ± 0.07	25.58 ± 0.07	24.68 ± 0.08	99	99	99	99	99
Lock850.018	99	99	99	99	99	99	99	99	99
Lock850.019	27.32 ± 0.17	24.93 ± 0.06	24.47 ± 0.06	24.52 ± 0.07	21.71 ± 0.08	21.06 ± 0.20	20.93 ± 0.19	20.83 ± 0.50	21.25 ± 0.59
Lock850.021	99	99	99	99	99	22.13 ± 0.33	22.13 ± 0.35	21.42 ± 0.70	22.37 ± 0.60
Lock850.022	23.65 ± 0.06	23.05 ± 0.06	22.82 ± 0.06	22.74 ± 0.06	21.77 ± 0.08	21.27 ± 0.19	21.01 ± 0.16	20.80 ± 0.40	21.07 ± 0.31
Lock850.023	25.47 ± 0.06	22.38 ± 0.06	21.25 ± 0.06	20.70 ± 0.06	19.06 ± 0.06	18.89 ± 0.20	19.51 ± 0.21	19.71 ± 0.31	20.75 ± 0.30
Lock850.024	24.61 ± 0.06	23.74 ± 0.06	23.14 ± 0.06	22.65 ± 0.06	20.52 ± 0.06	19.70 ± 0.20	19.59 ± 0.18	19.99 ± 0.32	20.62 ± 0.38
Lock850.026	26.95 ± 0.12	25.45 ± 0.12	25.30 ± 0.11	24.73 ± 0.10	22.70 ± 0.19	21.68 ± 0.27	21.37 ± 0.24	20.90 ± 0.62	21.83 ± 0.53
Lock850.027	23.77 ± 0.06	23.55 ± 0.06	22.78 ± 0.06	22.32 ± 0.06	21.18 ± 0.06	20.90 ± 0.20	21.00 ± 0.19	99	21.69 ± 0.45
Lock850.028	25.90 ± 0.06	24.60 ± 0.06	23.90 ± 0.06	23.27 ± 0.06	20.88 ± 0.06	20.29 ± 0.20	20.20 ± 0.17	20.35 ± 0.37	20.88 ± 0.36
Lock850.029	99	99	99	99	99	99	99	99	99
Lock850.030	25.89 ± 0.06	25.62 ± 0.10	25.27 ± 0.10	24.97 ± 0.08	99	21.81 ± 0.25	21.61 ± 0.24	99	99
Lock850.031	26.56 ± 0.09	25.81 ± 0.07	25.25 ± 0.06	24.94 ± 0.09	21.76 ± 0.07	20.44 ± 0.20	20.32 ± 0.20	20.20 ± 0.58	20.98 ± 0.50
Lock850.033	26.91 ± 0.20	26.08 ± 0.20	26.22 ± 0.20	25.93 ± 0.20	99	22.62 ± 0.33	22.12 ± 0.27	99	21.85 ± 0.68
Lock850.034	26.78 ± 0.11	24.91 ± 0.06	24.74 ± 0.06	24.35 ± 0.06	99	21.70 ± 0.28	21.45 ± 0.26	21.12 ± 0.64	21.41 ± 0.57
Lock850.035	99	99	99	99	99	99	99	99	99
Lock850.035b	24.65 ± 0.06	24.31 ± 0.06	23.83 ± 0.06	23.64 ± 0.06	21.74 ± 0.08	21.51 ± 0.21	21.33 ± 0.20	99	21.79 ± 0.55
Lock850.036	–	–	–	–	–	–	–	–	–
Lock850.037	99	99	99	99	99	99	99	99	99
Lock850.037b	25.81 ± 0.06	24.81 ± 0.06	24.09 ± 0.06	23.87 ± 0.06	21.14 ± 0.06	20.40 ± 0.18	20.23 ± 0.22	20.63 ± 0.43	21.32 ± 0.33
Lock850.038	24.28 ± 0.06	23.63 ± 0.06	23.12 ± 0.06	22.49 ± 0.06	20.82 ± 0.06	20.28 ± 0.20	20.02 ± 0.21	20.53 ± 0.33	20.71 ± 0.30
Lock850.039	–	–	–	–	–	–	–	–	–
Lock850.040	26.33 ± 0.07	25.95 ± 0.08	25.68 ± 0.08	24.97 ± 0.10	22.47 ± 0.16	21.21 ± 0.19	20.95 ± 0.23	20.69 ± 0.51	21.36 ± 0.45
Lock850.041b	24.42 ± 0.06	23.95 ± 0.06	23.53 ± 0.06	22.99 ± 0.06	–	21.25 ± 0.10	21.05 ± 0.22	20.42 ± 0.39	19.66 ± 0.37
Lock850.041	22.95 ± 0.06	22.05 ± 0.06	21.53 ± 0.06	21.05 ± 0.06	19.96 ± 0.06	19.27 ± 0.16	19.26 ± 0.19	19.53 ± 0.40	19.69 ± 0.34
Lock850.043	26.21 ± 0.06	25.18 ± 0.06	24.82 ± 0.06	24.48 ± 0.06	21.60 ± 0.07	21.19 ± 0.20	21.07 ± 0.19	20.88 ± 0.53	21.52 ± 0.42
Lock850.043b	23.66 ± 0.30	23.01 ± 0.15	22.46 ± 0.11	21.82 ± 0.06	20.14 ± 0.06	19.69 ± 0.16	19.52 ± 0.18	19.78 ± 0.36	20.39 ± 0.31
Lock850.047	26.51 ± 0.08	23.84 ± 0.06	23.23 ± 0.06	22.80 ± 0.06	21.95 ± 0.10	21.45 ± 0.18	21.65 ± 0.23	22.21 ± 0.58	99
Lock850.048	23.00 ± 0.06	21.47 ± 0.06	21.11 ± 0.06	20.62 ± 0.06	19.63 ± 0.06	19.73 ± 0.18	20.07 ± 0.21	20.53 ± 0.39	19.41 ± 0.32
Lock850.052	26.17 ± 0.06	24.56 ± 0.06	23.61 ± 0.06	22.88 ± 0.06	20.39 ± 0.06	19.30 ± 0.20	19.64 ± 0.19	20.25 ± 0.39	20.71 ± 0.30
Lock850.052b	99	26.88 ± 0.18	25.33 ± 0.06	24.90 ± 0.09	21.31 ± 0.06	19.92 ± 0.19	20.10 ± 0.20	20.52 ± 0.36	20.96 ± 0.39
Lock850.053	24.21 ± 0.06	23.92 ± 0.06	23.47 ± 0.06	23.19 ± 0.06	21.58 ± 0.06	20.96 ± 0.21	20.90 ± 0.18	21.09 ± 0.35	21.46 ± 0.40
Lock850.060	99	27.24 ± 0.24	27.77 ± 0.49	25.99 ± 0.24	23.44 ± 0.35	22.42 ± 0.37	22.04 ± 0.33	99	99
Lock850.063	99	24.57 ± 0.15	23.23 ± 0.06	23.11 ± 0.06	21.86 ± 0.08	20.98 ± 0.22	20.75 ± 0.20	20.51 ± 0.36	20.47 ± 0.38
Lock850.064	24.67 ± 0.06	24.05 ± 0.06	23.53 ± 0.06	22.97 ± 0.06	21.38 ± 0.06	21.16 ± 0.21	21.13 ± 0.20	21.35 ± 0.43	21.51 ± 0.41
Lock850.066	25.40 ± 0.06	25.06 ± 0.06	24.75 ± 0.06	24.49 ± 0.06	99	23.15 ± 0.52	23.10 ± 0.55	99	99
Lock850.067	28.41 ± 0.30	28.40 ± 0.50	26.58 ± 0.14	25.64 ± 0.14	99	22.00 ± 0.31	21.73 ± 0.30	22.38 ± 0.77	22.32 ± 0.68
Lock850.070	24.67 ± 0.05	23.10 ± 0.06	22.51 ± 0.06	22.41 ± 0.06	21.03 ± 0.06	21.13 ± 0.20	21.58 ± 0.28	21.28 ± 0.32	99
Lock850.071	25.43 ± 0.06	24.97 ± 0.06	24.76 ± 0.06	24.20 ± 0.06	21.76 ± 0.06	21.46 ± 0.25	21.05 ± 0.21	21.30 ± 0.35	99
Lock850.073	24.35 ± 0.06	23.63 ± 0.06	23.14 ± 0.06	22.67 ± 0.06	20.65 ± 0.06	20.33 ± 0.20	20.22 ± 0.18	20.36 ± 0.42	20.59 ± 0.36
Lock850.073b	24.94 ± 0.06	24.43 ± 0.06	24.07 ± 0.06	23.61 ± 0.06	21.79 ± 0.08	–	20.73 ± 0.19	–	20.78 ± 0.43
Lock850.075	25.57 ± 0.07	24.76 ± 0.06	24.23 ± 0.06	23.78 ± 0.06	22.13 ± 0.11	21.21 ± 0.21	21.00 ± 0.20	–	–
Lock850.076	23.23 ± 0.06	21.03 ± 0.06	20.22 ± 0.06	20.05 ± 0.06	19.00 ± 0.06	19.10 ± 0.17	19.47 ± 0.20	19.53 ± 0.33	19.36 ± 0.28
Lock850.077	27.02 ± 0.13	26.50 ± 0.13	25.86 ± 0.09	24.81 ± 0.08	99	22.23 ± 0.34	22.23 ± 0.36	99	99
Lock850.077b	27.59 ± 0.12	24.97 ± 0.06	24.62 ± 0.06	23.44 ± 0.06	21.14 ± 0.06	20.12 ± 0.20	20.03 ± 0.16	–	–
Lock850.078	24.84 ± 0.02	24.39 ± 0.06	24.03 ± 0.06	23.84 ± 0.06	22.39 ± 0.14	–	–	–	–
Lock850.079	26.39 ± 0.07	26.60 ± 0.14	25.54 ± 0.07	25.05 ± 0.10	22.06 ± 0.12	21.04 ± 0.20	20.79 ± 0.20	20.65 ± 0.51	20.52 ± 0.36
Lock850.081	23.75 ± 0.05	23.18 ± 0.06	22.65 ± 0.06	22.19 ± 0.06	20.07 ± 0.06	19.59 ± 0.19	18.90 ± 0.18	18.02 ± 0.20	17.20 ± 0.19
Lock850.083	21.27 ± 0.06	19.76 ± 0.06	19.41 ± 0.06	18.96 ± 0.06	18.38 ± 0.06	18.93 ± 0.18	19.21 ± 0.19	19.81 ± 0.21	18.61 ± 0.20
Lock850.087	26.70 ± 0.10	25.58 ± 0.07	24.86 ± 0.06	24.72 ± 0.08	21.82 ± 0.08	20.63 ± 0.21	20.02 ± 0.21	20.10 ± 0.39	20.21 ± 0.26
Lock850.100	23.87 ± 0.06	23.43 ± 0.06	23.16 ± 0.06	22.76 ± 0.06	21.36 ± 0.06	–	–	–	–

This paper has been typeset from a TEX/LATEX file prepared by the author.